RICE UNIVERSITY

Experiments and Modeling of Ternary Alloy Semiconductors

by

Stephanie E. Tritchler

A THESIS SUBMITTED
IN PARTIAL FULFILLMENT OF THE
REQUIREMENTS FOR THE DEGREE

Master of Science

APPROVED, THESIS COMMITTEE

Dr. Brent Houchens, Chair
Assistant Professor,
Mechanical Engineering and Materials Science

Dr. Yildiz Bayazitoglu
Professor,
Mechanical Engineering and Materials Science

Dr. Rob Griffin
Associate Professor,
Civil and Environmental Engineering

HOUSTON, TEXAS
January 2012

Abstract

Experiments and Modeling of Ternary Alloy Semiconductors

by

Stephanie Tritchler

Results of the growth of $Ga_{1-x}In_xSb$ crystals as the pseudobinary Ga_{1-x} Sb—In_xSb are presented. Special focus is given to the relationship between crystal composition and the cut-off wavelength of transmission for the crystal using Fourier Transform Infrared (FTIR) and Ultra Violet-Visual Wavelength (UV-Vis) spectroscopy. This provides a fast, easy method to determine the composition.

A Matlab model to determine the composition of a crystal grown using the Bridgman method is developed. This compares the ideal to the regular solution models for $Ga_{1-x}In_xSb$. These two models are used to predict the composition of the grown crystals. The regular solution yields a more accurate pseudo-binary phase diagram and thus a much closer fit to the experimental data.

Acknowledgments

First and foremost, I would like to thank Dr. B.C. Houchens, my advisor, for all his advice, help, experience, and, perhaps most of all, his patience.

I would also like to thank Andres Goza for his assistance and involvement during the summer research at Hanscom Air Force Base, as well as his Matlab skills in the comparison of the ideal and regular solution models.

Additionally, I'd like to thank Dr. David Bliss and the other members of the Air Force Research Lab Sensors Directorate at Hanscom Air Force base for all their help and advice.

The physical crystal research was supported by the U.S. Air Force Office of Scientific Research. I would also like to acknowledge generous support from AFRL through the Summer Researcher Program, administered by UTC under UTC prime contract FA8650-05-D-1912

Contents

Acknowledgments ..... **iii**

Contents ..... **iv**

List of Figures ..... **vi**

List of Tables ..... **viii**

List of Equations ..... **ix**

Introduction **10**

1.1. Motivation for Bulk Ternary Alloy Growth 10

1.2. Bulk Growth Methods 13

1.2.1. Travelling heater method 13

1.2.2. Bridgman growth 14

1.2.3. Czochralski method 15

1.3. Melt Growth 16

1.3.1. The effects of convection and mixing 16

1.3.2. Mixing via magnetic stirring 17

1.4. Modeling and Experiments Toward Bulk Ternary Growth 17

Experimental Procedure **19**

2.1. Synthesis 20

2.2. Horizontal Growth 23

2.3. Sample Preparation and Analysis 25

2.3.1. Cutting and Polishing 26

2.3.1. Spectroscopy 28

2.3.2. Bandgap Energy 31

2.3.3. Electron Microprobe 32
2.3.4. Experimental Error in Synthesis and Crystal Growth 33
2.3.5. Experimental Error in EMP Measurements 34
2.3.6. Experimental Error in Spectroscopy 34
Experimental Results of Horizontal Bridgman Growth 36
3.1. Electron Microprobe Results 36
3.2. InSb Crystal 38
3.3. Spectroscopy Results for $Ga_{1-x}In_xSb$ 39
3.4. Cutoff Wavelength vs. Composition and Bandgap Energy 42
3.5. Advanced Growth Techniques 45
Modeling the Solidification for Well-mixed Bridgman Growth 47
4.1. Ideal Solution Model 50
4.2. Improved pseudobinary phase diagram and the regular solution model 51
4.3. Computational Modeling 56
References 63
Appendix A: Additional data from the Bridgman growth and analysis 66
5.1. Additional electron microprobe data 66
5.2. Additional FTIR and UV-VIS data 69
5.3. Tables of cut-off wavelengths 71

List of Figures

Figure 1-1 The setup for Solute-feeding Czochralski method [16] 16

Figure 2-1 The horizontal Bridgeman furnace 23

Figure 2-2 End-on view of the furnace and quartz tubes 24

Figure 2-3 Temperature profile of horizontal growth heater with a set point of 640 °C 24

Figure 2-4 The wire saw cutting the $Ga_{50}In_{50}Sb$ sample 26

Figure 2-5 Axial slices of $Ga_{50}In_{50}Sb$ sample just after cutting. Graph paper is 10 squares per cm, overall crystal is 5-6 cm long 27

Figure 2-6: Axial slice of $Ga_{30}In_{70}Sb$ (center) surrounded by scrap pieces of InSb. Crystal grains can be seen in the $Ga_{30}In_{70}Sb$ piece 28

Figure 2-7 The MatLab plot of the percent transmission data obtained from the FT-IR spectrometer, the curve that was plotted to fit the region with the greatest change in percent transmittance, and cut-off point for the $Ga_{.30}In_{.70}Sb$ sample at 14 mm from the head of the crystal, which was calculating using Figure 2-8 30

Figure 2-8: The derivative of the curve fit shown in Figure 2-7 for $Ga_{.30}In_{.70}Sb$ sample at 14 mm from the head of the crystal, with the maximum (and therefore cut-off wavelength) marked 31

Figure 3-1 Electron microprobe data for $Ga_{70}In_{30}Sb$ 37

Figure 3-2 Plot of FTIR data for $Ga_{70}In_{30}Sb$ 41

Figure 3-3 The UV-VIS data for $Ga_{70}In_{30}Sb$ 41

Figure 3-4 The FTIR plot for $Ga_{30}In_{70}Sb$ 42

Figure 3-5 Plot of bandgap energy versus gallium percentage, using crystals of 30% Ga, 50% Ga, and 70% Ga measured at different horizontal locations compared to bowing parameter from [23] 44

Figure 3-6 Cumulative Error bars for Gallium percentage 45

Figure 3-7 EMP data from the HTHM crystal, also found in [6] 46

Figure 4-1 An ideal solution model pseudobinary phase diagram for $Ga_{1-x}In_xSb$ 48

Figure 4-2 The ideal and regular solution pseudobinary phase diagrams for $Ga_{1-x}In_xSb$ 54

Figure 4-3 Comparison of Ideal and Regular Solution models to EMP data for $Ga_{70}In_{30}Sb$ 57

Figure 4-4 Comparison of Ideal and Regular Solution models to EMP data for $Ga_{50}In_{50}Sb$ 58

Figure 4-5 Comparison of Ideal and Regular Solution models to EMP data for $Ga_{30}In_{70}Sb$ 59

Figure 4-6 Comparison of regular solution model with modified beginning massses to the Ideal model, Regular Solution model, and EMP data for $Ga_{70}In_{30}Sb$ 61

Figure 4-7 Comparison of Regular Solution model with modified beginning massses to the Ideal model, Regular Solution model, and EMP data for $Ga_{50}In_{50}Sb$ 62

Figure 4-8 Comparison of Regular Solution model with modified beginning massses to the Ideal model, Regular Solution model, and EMP data for $Ga_{30}In_{70}Sb$ 62

Figure 5-1 Electron microprobe data for $Ga_{30}In_{70}Sb$ 67

Figure 5-2 Electron microprobe data for $Ga_{50}In_{50}Sb$ 68

Figure 5-3 FTIR data for $Ga_{30}In_{70}Sb$ 69

Figure 5-4 FTIR and UV-VIS data for $Ga_{50}In_{50}Sb$ 70

List of Tables

Table 2-1 Starting masses of gallium, indium, and antimony for $Ga_{30}In_{70}Sb$, $Ga_{50}In_{50}Sb$, and $Ga_{70}In_{30}Sb$ experiments 20

Table 3-1 Cutoff wavelength compared to %Ga in the InSb crystal 39

Table 3-2 Spectroscopy data for $Ga_{70}In_{30}Sb$, showing the distance from the head, cut-off wavelength, atomic percentage of gallium, and the calculated bandgap energy 43

Table 5-1 Spectroscopy data for $Ga_{30}In_{70}Sb$, showing the distance from the head, cut-off wavelength, atomic percentage of gallium, and the calculated bandgap energy 71

Table 5-2 Spectroscopy data for $Ga_{50}In_{50}Sb$, showing the distance from the head, cut-off wavelength, atomic percentage of gallium, and the calculated bandgap energy 72

List of Equations

Equation 2-1 ..... **21**

Equation 2-2 ..... **21**

Equation 2-3 ..... **32**

Equation 4-1 ..... **47**

Equation 4-2 ..... **50**

Equation 4-3 ..... **50**

Equation 4-4 ..... **51**

Equation 4-5 ..... **51**

Equation 4-6 ..... **51**

Equation 4-7 ..... **52**

Equation 4-8 ..... **52**

Equation 4-9 ..... **53**

Equation 4-10 ..... **53**

Equation 4-11 ..... **53**

Equation 4-12 ..... **54**

Equation 4-13 ..... **54**

Equation 4-14 ..... **55**

Equation 4-15 ..... **55**

Equation 4-16 ..... **56**

Equation 4-17 ..... **56**

Chapter 1

Introduction

1.1. **Motivation for Bulk Ternary Alloy Growth**

Semiconductors are an important part of our technological base and are used to perform many tasks. While silicon is widely used, in large part due to its ease of growth, other semiconductors and alloy materials are being developed for advanced applications. The constitutive elements of a semiconductor determine its function and properties. As such, much research has been done on the growth of specific types of semiconductors, with most studies focusing on either binary alloys, such as GaAs [1], or ternary alloys, such as GaInSb, GaInAs, and AlInSb [2]. Growth of such alloys involves manipulation of the bandgap energy of the material. Bandgap energy is the energy needed to excite an electron and cause it to jump from the valence band into the conduction band. Each element has its own unique bandgap energy.

By alloying elements together in specific concentrations one can change the effective bandgap energy of the material.

Because every bandgap energy corresponds to the energy carried by photons of a certain wavelength, each semiconductor and alloy composition has specific optoelectric properties. By tuning bandgap energies, it is possible to create lasers and photo-emitters which operate at specific wavelengths [3], or create photodectectors which are sensitive to specific wavelengths [4]. Additionally, these crystals can provide lattice-matched substrates for epitaxial film growth of devices ranging from ultra high-speed electronics to efficient solar cells to photoconductive radiation detectors.

Substrates in the narrower bandgap range are useful for optical and thermo-photovoltaic sensors and devices, and those in the wider range have applications in IR detectors for defense applications and homeland security. For example, high quality CdZnTe can be used for short wavelength x-ray and gamma-ray detection at room temperature. CdZnTe sensors are ideal for detecting nuclear material such as would be present in dirty bombs, and have the advantage of room temperature photoconductive operation. Other simpler materials such as germanium require liquid nitrogen cooling for such sensing applications, making them expensive or impractical to operate. Sensors need to be sufficiently inexpensive to allow for wide-spread and redundant implementation at shipping ports and transportation hubs. Only cost effective bulk production can provide ample substrates to meet the demand for these devices.

The incorporation of a third alloying element into a semiconductor can allow for more finely tuned control over the properties, and therefore, its application. However, actually growing these ternary crystals is no small feat, as multiple factors – growth rates, interface shape, the mechanisms of solute rejection, buoyant convention and interface breakdown leading to polycrystalline growth – all affect the growth and composition of the crystals [2]. Because of the complicated nature of the growth mechanism, a multitude of different growth methods have been developed over the past three decades as the field of group III-V ternary semiconductor growth has become of interest. However, these methods are slow and expensive, limiting the impact of alloyed semiconductors in industrial and commercial markets.

In this research ternary alloy $Ga_{1-x}In_xSb$ crystals were grown and the solidification segregation was modeled to predict the final axial composition of the crystals given the initial concentrations and growth parameters. This work is the first step toward developing inverse models which can quickly and inexpensively predict the initial and growth conditions needed to grow semiconductor crystals of a desired final composition. This will reduce the need for energy intensive, time consuming experiments (often taking months) performed in a trial-and-error methodology, using expensive materials.

The ternary system studied here is GaInSb. The bandgap for this alloy can be continuously tuned from 0.726eV (GaSb) to 0.17eV (InSb). The narrow bandgap range is ideal for optical and thermo-voltaic applications and the larger bandgap

range is relevant for IR detectors and super high-speed terahertz electronics. Both experimental results and models are presented to better understand ternary alloy growth based on this system.

The processing techniques and models investigated here are also relevant to CdZnTe, another ternary system of great interest. The ultimate goal of this research is to grow single crystals at a controlled composition, yielding the exact bandgap required for the optoelectronic application of interest.

1.2. **Bulk Growth Methods**

1.2.1. Travelling heater method

Yip and Wilcox began the study of the growth of group III-V semiconductors with the growth of GaAs, $Ga_xIn_{1-x}Sb$, and $Ga_xAl_{1-x}Sb$ by the Travelling Heater Method (THM) [1]. As the name implies, THM is a method whereby a heater is translated along the length of a crystal, causing a solvent zone to move through a solid feed material. Material is melted at one end of the solvent zone, and is recrystalized at the other end, ideally as a single crystal with a more uniform composition. THM can be used to grow crystals vertically [1][5], or horizontally [6]. Additionally, the heater itself can remain stationary while the crystal is moved through the furnace, as in Yip and Wilcox [1], where the ampoule was lowered through the center of the stationary furnace. A more general definition of the method would be that in each case, the relative positions of the heater and the crystal material change with respect to one another.

This method has been shown to reduce the supercooling commonly found in standard isothermal solution growth, however this change can lead to an increase in convection in the melt [7]. This may or may not be desirable, depending on the intended purpose of the crystal being grown.

A similar, yet slightly different mechanism of growth is known as the Travelling Liquid Zone method (TLZ)[8-12]. TLZ uses a compositionally gradated feed crystal as the source for replenishing the melt in an attempt to keep the melt composition constant. Research into TLZ growth of alloyed crystals has been fairly comprehensive, especially with regards to $In_xGa_{1-x}As$ alloys. A single crystal of $In_{0.30}Ga_{0.70}As$ was grown using this method [9], though the crystal was only 2mm in diameter and approximately 20mm in length. In order to grow a single crystal of a specific composition, the material must translate through the furnace at the same rate as the crystal grows. At first, the optimal growth rate was determined experimentally [9], but later investigations led to a numerical model through which the growth rate could be determined [12]. The effect of latent heat on the crystal growth [11] was also investigated, finding that TLZ method of growth may break down if the growth rate surpasses 0.46 mm/h for $In_xGa_{1-x}As$.

1.2.2. Bridgman growth

Another crystal growth method that falls into a similar category as the THM/TLZ methods is known as Bridgman growth. This method also involves a change in relative position between the furnace and the material being melted, however, in this method, the entirety of the sample is melted at the beginning of the

process, instead of only a small portion at a time. As one might expect, with only slight differences in procedure from the THM/TLZ methods, the Bridgman technique is also a very versatile growth method, as crystals can be grown in a variety of orientations [6], [13], with magnetic [14] or physical stirring [15] or none, and with or without a seed crystal.

1.2.3. Czochralski method

Whereas the first three methods discussed above are all quite similar in nature, the Czochralski method (CZ) uses a completely different type of arrangement for crystal growth. The material is melted in a large crucible, into which a seed crystal is dipped and slowly withdrawn while rotating. Speed of rotation, temperature, and rate of withdrawal all determine the diameter of the resulting crystal. This method is especially well-known for growing large single crystal ingots of silicon for microchips and solar cells. There are drawbacks to the basic CZ method – specifically, in alloy growth, preferential solidification of one element can cause depletion from the melt, leading to variation in composition along the length of the forming crystal.

Solute-feeding CZ addresses this concern by attempting to develop a control mechanism for the transport of solute from the source to the crystal's growth front, thereby allowing for the formation of crystals with less compositional variation along their length [16]. In this technique, a buffer is placed between the source region – where the material for the melt is obtained – and the growth front, and only a small amount of solute from the source region is allowed to pass to the growth

front, establishing conditions suitable for stable CZ-mode growth at the interface [16]. Figure 1-1, shown below as taken from [16], outlines the basic growth setup for solute-feeding CZ. Changing the diameter of the connecting passage between the source region and the growth front changes the solute supply rate and accordingly can affect the composition of the crystal [16].

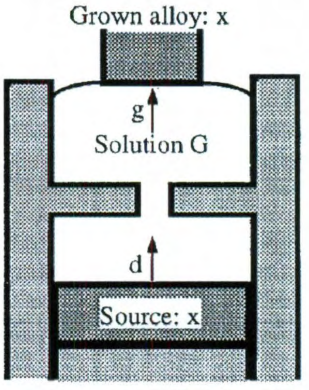

Figure 1-1 The setup for Solute-feeding Czochralski method [16]

1.3. Melt Growth

1.3.1. The effects of convection and mixing

A number of studies have examined the effects of convection in the melt upon the composition of the growing crystal. In theory, convection can help grow crystals of more consistent composition. In a system with a greater amount of convection mixing is enhanced within the melt, thereby both replenishing the solute at the growth interface and minimizing the impact of segregation [14]. Some research has been done on ways to increase physical mixing through other means, such as

magnetic stirring. Kim et al. [15] found that increasing mixing can substantially improve the homogeneity of radial composition in $Ga_{1-x}In_xSb$ crystals. Convection has also been shown to reduce cracks in the final crystals [17].

However, other research has sought to eliminate convection [18] as it can disrupt the growth interface and lead to polycrystalline end products. Convection can also disrupt steady replenishment of 'impurities' at the growth interface due to the fact that convection on earth is buoyancy driven and therefore rarely steady or predictable [19].

1.3.2. Mixing via magnetic stirring

Magnetic stirring has also been investigated as a way to increase the mixing of the melt and prevent the depletion of materials at the growth interface [20][14]. Magnetic stirring used in conjunction with the Bridgman method has been used to improve the composition of the final crystal [14]. The use of magnetic fields also show promise in producing more uniform crystals by stabilizing flow in the melt [21]. Additionally, by mixing the material at the growth interface, magnetic stirring can lessen the interface curvature [14]. This method has been proven to grow highly uniform $Ga_{1-x}In_xSb$ crystals [22].

1.4. Modeling and Experiments Toward Bulk Ternary Growth

Semiconductor ternary alloys of interest here, with constant composition and high quality microstructure, have not been successfully grown in bulk. Most growth

methods are slow and very sensitive to initial and boundary conditions, and suffer from either nonuniform composition (either radial, axial or both) and microstructure defects including twins and precipitates.

This work sought to first verify the segregation of GaSb in the growth of GaInSb through Bridgman experiments. The method of growth is described below in Chapter 2: Experimental Procedure. Chapter 3: Experimental Results of Bridgman Growth details the characterization methods used to determine the composition of the grown crystals. The grown crystals are compared to segregation models for growth from a well-mixed melt in Chapter 4: Modeling the Solidification for well-mixed Bridgman Growth.

Chapter 2

Experimental Procedure

The experimental data presented are from three crystals which were grown by the horizontal Bridgman travelling heater method; $Ga_{30}In_{70}Sb$, $Ga_{50}In_{50}Sb$, and $Ga_{70}In_{30}Sb$. This experimental procedure consisted of three steps: vertical synthesis, horizontal growth, and analysis. In the synthesis step, gallium, indium, and antimony were measured out in the correct proportions, then melted, mixed, and quenched. Horizontal growth was performed using the horizontal Bridgman technique. As discussed previously, in Bridgman growth the entire charge is melted and then directionally solidified by allowing it to cool from one end. For analysis the crystals were sliced and polished to determine the composition along the length of the crystal.

2.1. Synthesis

A quartz tube with a diameter of 11mm was sealed at one end to be used as an ampoule. A smaller tube was also sealed at one end to act as a plug. The gallium, indium, and antimony were then weighed out to the correct proportions.

Crystal	Mass of Ga (g)	Mass of In (g)	Mass of Sb (g)
$Ga_{30}In_{70}Sb$	2.01	7.71	11.68
$Ga_{50}In_{50}Sb$	3.49	5.74	12.18
$Ga_{70}In_{30}Sb$	5.09	3.59	12.70

Table 2-1 Starting masses of gallium, indium, and antimony for $Ga_{30}In_{70}Sb$, $Ga_{50}In_{50}Sb$, and $Ga_{70}In_{30}Sb$ experiments

The gallium was weighed out first, as it is the most difficult element to handle. The gallium came in a plastic squeeze bottle was heated to a melt. Beads of gallium were then squeezed out into small boats made from cutting plastic pipette bulbs in half lengthwise. These boats were small enough to slide into the ampoule, and thus could guarantee that the beads of gallium would fit as well. The boats were placed in a freezer to solidify the gallium. These gallium beads were then weighed. Beads weighing roughly 2 grams, 3.5 grams, and 5 grams were selected for the three

alloys. From this mass the number of moles of gallium was calculated using $Moles_{Ga} = mass_{Ga}/molarMass_{Ga}$ with a molar mass of 69.723 g/mol for Ga.

Once the moles of gallium were known, the desired moles of indium and antimony were calculated using Equation 2-1 and Equation 2-2, where $\%In$ is equal to the desired percentage of moles of InSb. From these molar amounts and using molar masses of 114.818 g/mol for In, and 121.760 g/mol for Sb, the target masses of indium and antimony were calculated using the relationship $mass_{element} = moles_{element} * molarMass_{element}$. Table 2-1 shows the measured initial masses of each element for the three experiments. The moles of In are given by

$$moles_{In} = moles_{Ga} * \left(\frac{\%In}{\%Ga}\right)$$

Equation 2-1

$$moles_{Sb} = moles_{Ga} + moles_{In}$$

Equation 2-2

Small pieces of indium were clipped from larger billets using wire cutters, which had been ultrasonically cleaned to remove impurities. These chunks were then weighed to find a suitable combination for the total mass of indium needed. A chunk of antimony was lightly crushed in a mortar and pestle, which was used

exclusively for antimony. The pieces produced from the crushing were small enough to fit into the ampoule. As with indium, pieces of antimony were weighed to find a match to the required masses.

The indium and antimony chunks were placed into the ampoule, alternating to get a decent pre-melt mix. After roughly half the indium and antimony was layered into the tube, a bead or two of the gallium was placed on top and then held near the vertical furnace to let it melt and fill in the spaces around the indium and antimony. The rest of the indium and antimony were placed in the ampoule, again alternating the materials and this was topped off with the rest of the gallium which was similarly melted.

The filled ampoule with its plug was then placed on a vacuum pump and the air was drawn out of the ampoule. As the ampoule was horizontal, care had to be taken when starting the pump to prevent the air rushing out of the ampoule from pulling the plug and the sample into the pump itself. While under vacuum, the ampoule was sealed to the plug using an oxyhydrogen torch. A long quartz hook was then attached to the end of the sealed ampoule. The ampoule was then hung in a vertical furnace and the temperature raised above the liquidus for 16 hours to allow the melt to mix thoroughly by diffusion. After the synthesis, the ampoule was lowered quickly out of the hot-zone in the furnace, allowing the melt to cool from one end to reduce the chance of the ampoule breaking as the melt solidified. This quenching was done relatively rapidly to limit differentiation along the length of the

crystal. The vertical synthesis produced a well-mixed ingot of the proper shape to fit into the horizontal growth ampoule.

2.2. **Horizontal Growth**

After the sample cooled completely, the ampoule was carefully scored and broken to retrieve the sample. The sample was lightly ground and then etched with a mixture of HCl, HNO_3, and deionized water [6] to remove oxides and then placed in a desiccant jar to dry, along with a new quartz ampoule and plug. The sample was then placed in the ampoule with the plug as described before, and then was attached to the vacuum pump for an hour before being sealed as before, but without a hook.

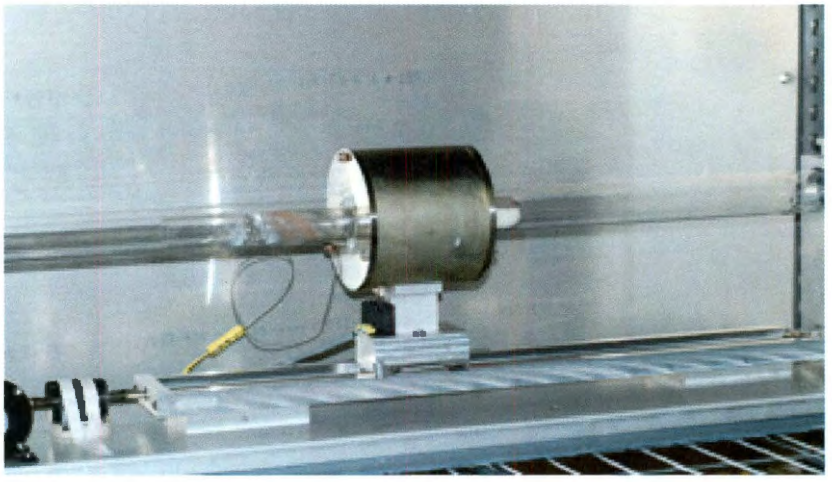

Figure 2-1 The horizontal Bridgeman furnace

The sample was then placed inside a large horizontal quartz tube to support the sample and offset it below the axis of the cylindrical furnace, as shown in Figure 2-1. A schematic of the end view is shown in Figure 2-2

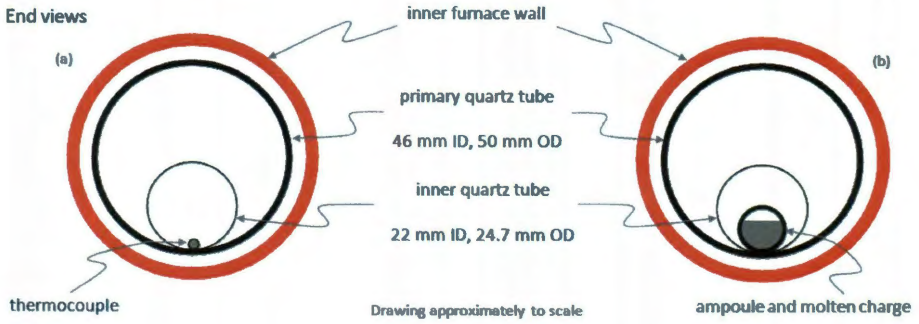

Figure 2-2 End-on view of the furnace and quartz tubes

The quartz tube and the ampoule remained stationary while the cylindrical heating element translated horizontally. The heating element was approximately 5 cm long, and provided a roughly parabolic temperature profile as seen in Figure 2-3.

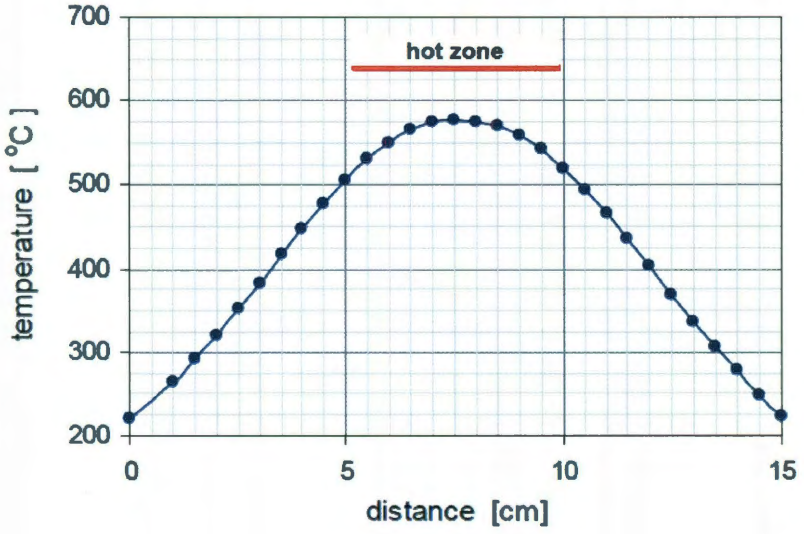

Figure 2-3 Temperature profile of horizontal growth heater with a set point of 640 °C

The temperature was raised to well above the liquidus temperature for the particular $Ga_{1-x}In_xSb$ composition. For example, for $Ga_{50}In_{50}Sb$ the furnace was maintained at a set point of 890 °C corresponding to a maximum temperature of approximately 780 °C just outside the ampoule. Once the whole sample was molten, it was allowed to mix again for a minimum of 12 hours. The motor was then turned on, translating the furnace along the length of the crystal. Solidification began at the end which first exited the hot-zone of the furnace and propagated along the sample as the furnace moved. The growth rate was 0.9 mm/hr, determined by the length of the charge and the diffusion rate of Ga in InSb. Because of the scatter in the reported diffusion rates, the speed was set between 2 and 5 times below the time estimated for gallium to replenish from the tail to the head of the crystal.

2.3. **Sample Preparation and Analysis**

The final step of our experiment was to analyze the crystals grown. We specifically were interested in examining how the change in composition affects the crystal's physical properties, including bandgap energy. As the crystals were assumed to be pseudobinary, the percentage of gallium in the crystal was treated as the independent variable. The stoichiometric amount of gallium in the crystal directly related to the amount of GaSb 'material' in the binary alloy and determined the amount of InSb in the crystal as well.

2.3.1. Cutting and Polishing

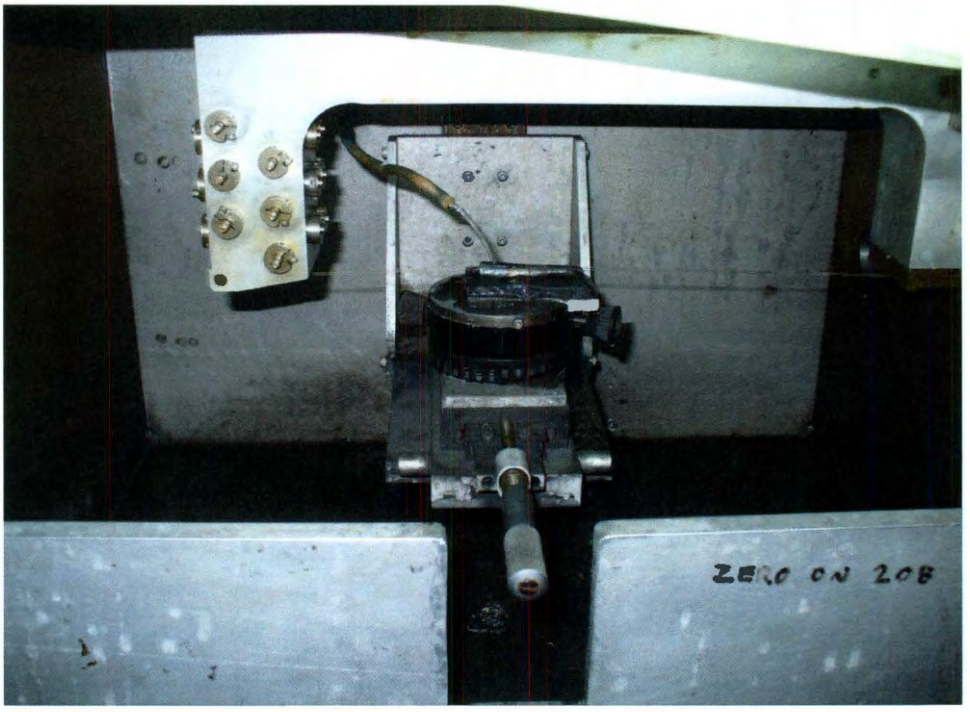

Figure 2-4 The wire saw cutting the $Ga_{50}In_{50}Sb$ sample

Once the growth of the crystal was completed, the samples were removed from the furnace and cut on a special horizontal wire saw, which cut two axial slices out of the center of the crystal (see Figure 2-5 below). One slice was 2.04 mm thick and was polished on both sides to be used for Fourier Transform Infrared (FTIR) and Ultra Violet-Visual Wavelength (UV-VIS) spectroscopy, while the other slice was 1.78 mm thick and polished only on one side for Electron Microprobe (EMP) analysis.

Figure 2-5 Axial slices of $Ga_{50}In_{50}Sb$ sample just after cutting. Graph paper is 10 squares per cm, overall crystal is 5-6 cm long.

Each sample was individually mounted on glass discs using Crystal Bond (see Figure 2-6 below) a clear adhesive which is heat activated. Scrap InSb crystal material was also mounted on the plates to help support the glass disk while lapping and to prevent the GaInSb crystals from becoming thinner on one edge, as seen in Figure 2-6. The crystals were lapped by hand on a lapping plate using progressively finer grains of Alumina lapping grit. They were then polished to a mirror finish using a polishing wheel with polishing pad and diamond liquid suspension. The thicker pieces were then removed from the disks, flipped over, and the lapping and polishing process repeated for the spectroscopy methods mentioned earlier, while the thinner pieces were taken to undergo EMP.

Figure 2-6: Axial slice of $Ga_{30}In_{70}Sb$ (center) surrounded by scrap pieces of InSb. Crystal grains can be seen in the $Ga_{30}In_{70}Sb$ piece

2.3.1. Spectroscopy

Fourier Transform Infrared Spectroscopy (FTIR) and Ultra Violet-Visual Wavelength Spectroscopy (UV-Vis) were used as a means of analyzing the dual-polished samples that were prepared as described above. Roughly six measurements were taken along the length of each crystal. UV-VIS Spectroscopy was performed on the points of the crystal where FTIR was unable to measure the cut-off wavelength. FTIR was able to measure wavelengths of 2.5-25 μm while UV-VIS measured wavelengths of 1.8-2.5 μm. Spectroscopic measurements were also taken of a pure indium-antimonide (InSb) sample as a baseline to verify the cut-off wavelength of a crystal with no gallium present.

Once the transmission was obtained from the FTIR, the peak wavelength, or cut-off wavelength, was calculated for each sample. The importance of the cut-off wavelength will be discussed in more detail in the next section, but in general terms, it marks the point at which the crystal begins to absorb light instead of simply transmitting it, and it is tied to the physical capabilities of a semiconductor.

The actual calculation of the cut-off wavelength was achieved by importing the data produced by spectroscopy into Matlab, and calculating a polynomial equation to fit the curve in a region on the percent transmission spectrum where there was a dramatic increase in the percent transmission. Once a curve had been fit to this section of the plot, we were able to find the cut-off wavelength by taking the derivative of our fitted curve and finding its maximum value.

The following figures (Figure 2-7 and Figure 2-8) show the Matlab plots produced for the $Ga_{0.30}In_{0.70}Sb$ sample at 14 mm from the head of the crystal. At this location, the FTIR was used to find the cutoff wavelength, which under these circumstances was 3.3568 μm.

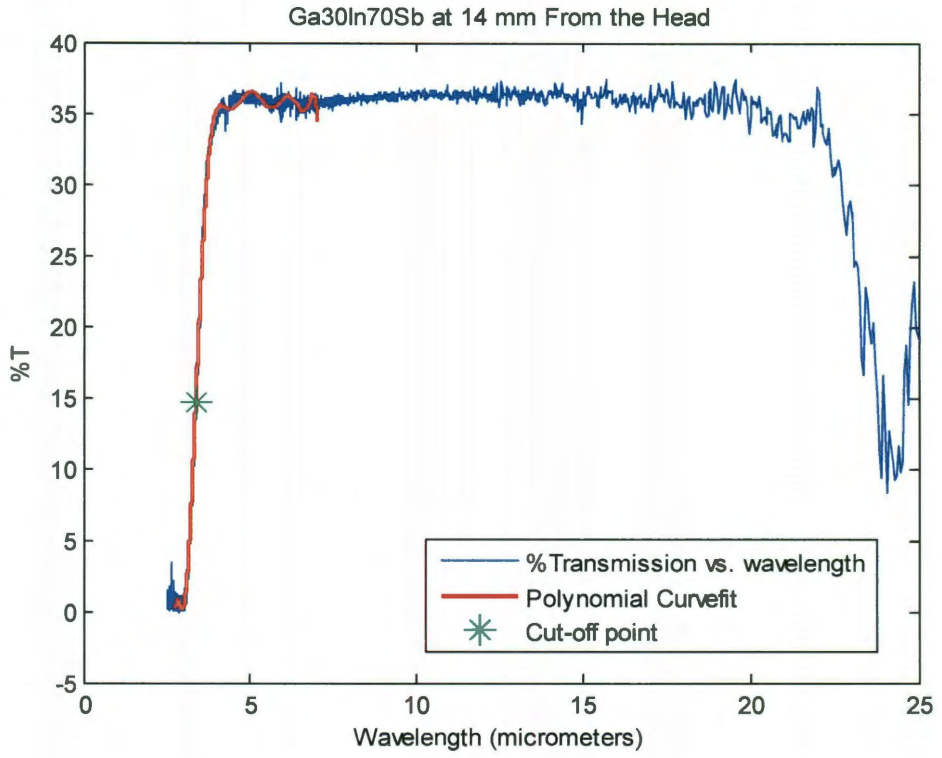

Figure 2-7 The Matlab plot of the percent transmission data obtained from the FT-IR spectrometer, the curve that was plotted to fit the region with the greatest change in percent transmittance, and cut-off point for the $Ga_{.30}In_{.70}Sb$ sample at 14 mm from the head of the crystal, which was calculating using Figure 2-8

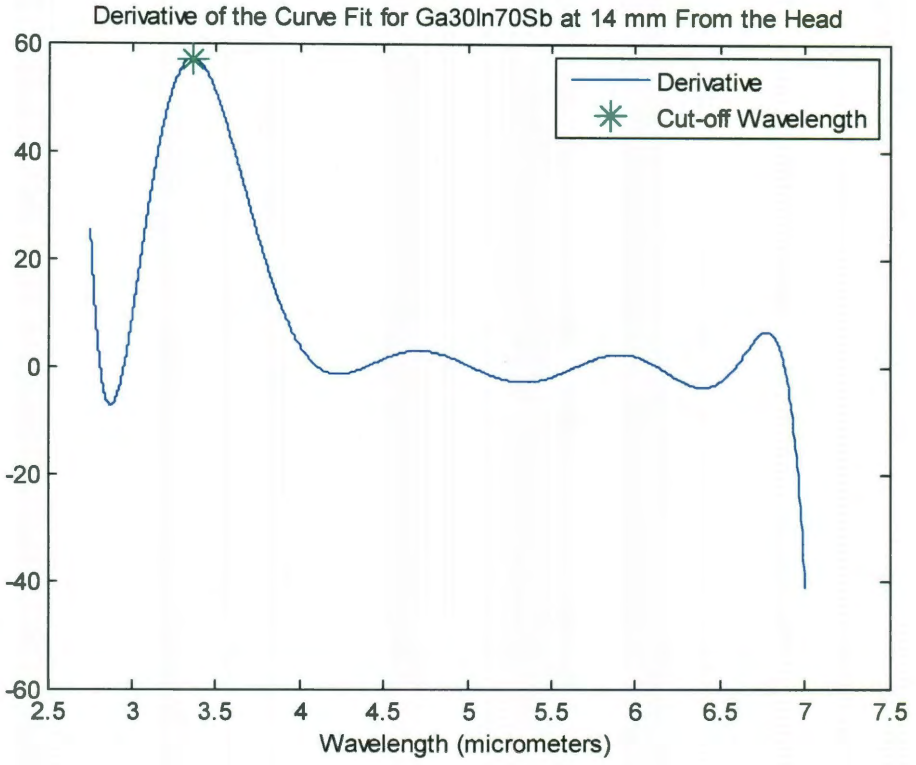

Figure 2-8: The derivative of the curve fit shown in Figure 2-7 for $Ga_{.30}In_{.70}Sb$ sample at 14 mm from the head of the crystal, with the maximum (and therefore cut-off wavelength) marked

2.3.2. Bandgap Energy

Bandgaps, more properly known as bandgap energies, represent the energy needed to excite an electron and cause it to jump from the valence band into the conduction band. Each element has a unique bandgap energy. By combining different elements together, one can change the effective bandgap energy of the material. This also means that specific wavelengths of light will be absorbed by the material, as photons hit the electrons and are absorbed, giving the electrons enough

energy to jump into the conduction band. The bandgap energy is related to the wavelength by Equation 2-3, where c is the speed of light, h is Planck's constant, the energy is in eV, and the wavelength is measured in microns.

$$Bandgap\ energy\ (eV) = \frac{hc}{\lambda(microns)} \cong \frac{1.24}{\lambda(microns)}$$

Equation 2-3

The cut-off wavelength found by spectroscopy in 2.3.1 is the wavelength entered into this equation, as this peak wavelength is the wavelength where the material absorbs the photons. This can allow tailoring of semiconductor alloys for specific uses, such as light emitters including lasers and diodes or photodetectors of a specific wavelength. Additionally, a material's cut-off wavelength is related to its bandgap energy, and a crystal's bandgap energy can be changed based on composition. Thus a relationship between cut-off wavelength and composition exists. This correlation allows researchers to use FTIR/UV-VIS to roughly determine a grown crystal's composition at any point without having to analyze the crystal with costly and time intensive electron microprobe.

2.3.3. Electron Microprobe

Electron Microprobe was performed by Geller Microanalytical Lab. Measurements were taken every 1mm axially along the length of the crystal slice. EMP was performed to determine the true composition of the crystal along its

length. As with spectroscopy, the InSb crystal was also analyzed by electron microprobe as a control. Sources of Experimental Error

There are several sources of experimental error. These occur in both synthesis and growth, and characterization steps.

2.3.4. Experimental Error in Synthesis and Crystal Growth

The first source of error involves the initial measurement of materials for synthesis. The scale used to weigh out the elements had an accuracy of 0.01 grams, and this combined with using small chunks of material, means that the number of moles of each material did not exactly reach proportions of $Ga_{70}In_{30}Sb$, $Ga_{50}In_{50}Sb$, or $Ga_{30}In_{70}Sb$.

Once synthesis was complete, as mentioned in Section 2.1, the charge was ground and etched to remove oxidation. This means that more material was removed, and it is unlikely that it was removed in proportionate amounts (*e.g.* potentially say 35% of what was removed was Ga in the $Ga_{70}In_{30}Sb$ run). Because indium is preferentially rejected during solidification, there were cases where small In rich beads formed at the end of the charge which were then lost during this grinding and etching process. Unfortunately, it is impossible to know exactly how many moles of each element were lost in this process. To account for this, an improved measure of the final crystal composition was extracted by integrating the EMP data, though this also has a smaller magnitude source of error as discussed below. The predictions of the regular solution model in the next chapter include

both the starting mass and modified mass predictions, bounding the range of possible outcomes.

2.3.5. Experimental Error in EMP Measurements

During the EMP measurements, the composition was measured near the center of the sample. In data presented to us by Geller Microanalytical Lab, the measured total compositions varied from 99.3 to 101.3 %, which leads to an error estimate of approximately ± 1%. These errors occur when the electron microprobe is not perfectly focused, due to slight curvature of the sample surface. Additionally, though it was requested that EMP measurements be taken each millimeter along the central axis, it is unclear whether they were taken with the first measurement exactly at the beginning of the crystal, 1mm back from the head, or somewhere in between, therefore there is also an error of roughly ±1 mm in the position of the EMP measurements.

2.3.6. Experimental Error in Spectroscopy

The apertures of the spectroscopes were roughly 0.5 cm by 0.5 cm, leading to a much larger sample area of material at each measurement point, as compared to the EMP sampling area. The resultant composition measurement at each point is essentially an average over the entire area. While this isn't a major issue at the ends of a crystal, during the turnover point where there is a rapid change in composition the readings are an average of an area with large deviation from edge to edge. Additionally, some of the crystals broke into multiple pieces. Though it was possible

to reassemble the crystal to ensure proper locations were sampled, not all of the measurements could be taken along the axis of the crystal. This coupled with the need to avoid the fractures resulted in variations of ±0.02 mm in the position measurements. The compounded errors from the spectroscopy measurements are demonstrated in the next chapter in Figure 3-6.

Chapter 3

Experimental Results of Horizontal Bridgman Growth

Graphs of the EMP data, spectroscopy, and comparisons between composition and bandgap energy for the crystals grown through Horizontal Bridgman method are presented below. The bowing parameter, linking the composition of the crystal and the cut-off wavelength, was reconfirmed.

3.1. **Electron Microprobe Results**

Upon completion of the EMP testing, Geller Microanalytical Lab returned a spreadsheet detailing the composition of the crystals by both element weight and atomic percentages at each specific position tested. The data are plotted here to show the composition of the crystals along their length. Element weight percentage refers to how much of the crystal mass at that point is due to a specific element.

Atomic percentage, by contrast, refers to the percentage of atoms of that element at that point. Figure 3-1 shows the electron microprobe data for $Ga_{70}In_{30}Sb$; the top graph is the element weight percentage while the bottom is atomic percentage. The graphs for the other two composition crystals can be found in the appendices in Figure 5.1. For all $Ga_{1-x}In_xSb$ crystals, as the distance from the head of the crystal increased, the percentage of gallium decreased slightly until the melt was significantly depleted of gallium, at which point the percentage of gallium decreased sharply. As can be seen in the figures below, gallium tends to be preferentially rejected from the liquid, and a high-percentage gallium crystal grows first.

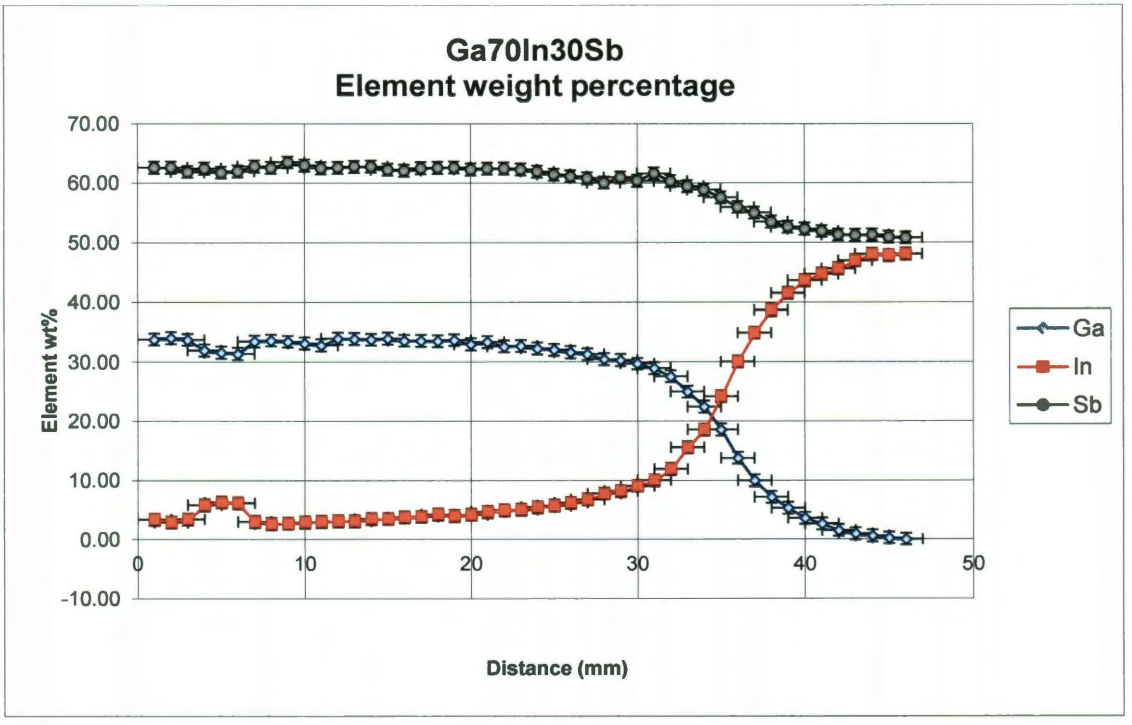

Figure 3-1 Electron microprobe data for $Ga_{70}In_{30}Sb$

Figure 3-1 shows the typical error in the EMP measurements, both in the position and composition reading. For composition, there is a baseline level of error in the EMP readings, from both sample curvature and presence of trace contaminants, amounting to -1% to +1.3% and represented by the vertical error bars. There is also an error associated with positioning of the probe associated with the horizontal errors bars. This has the greatest impact on the total possible error around the transition from high Ga to high In composition. It should be noted that our crystals broke into at least two parts. This, coupled with the fact that the first EMP measurements were not taken exactly at the head of the crystal but instead could have been between 0 and 1 mm in, may shift the data slightly along the x-axis, however the overall trends would remain unchanged.

3.2. **InSb Crystal**

The first crystal analyzed was pure InSb, which could also be thought of as $Ga_{0.0}In_{1.0}Sb$. The InSb crystal was nearly uniform without major fluctuations in composition. It was thus expected that the cutoff wavelength in a crystal of pure InSb would be constant.

Distance from head (mm)	Wavelength of peak of derivative (μm)
4.62	8.0321
10.30	7.9872

15.22	8.0064
24.22	7.9365
28.08	7.8989
34.90	7.8989

Table 3-1 Cutoff wavelength compared to %Ga in the InSb crystal

As can be seen in Table 3-1, which compares spectroscopy data to electron microprobe data for indium-antimonide, there was little difference in the peak wavelength. This demonstrates that the spectroscopy data collection was performed correctly and gives some indication of the inherent error in the method. Most of this variation is likely due to slight changes in the composition of the InSb crystal due to small pockets of indium or antimony rich material. In the worst case, the variation is the error in the spectroscopy measurements and associated curve fit, indicating that determination of the wavelength of the peak derivative by spectroscopy has an error of ±0.067 μm.

3.3. Spectroscopy Results for $Ga_{1-x}In_xSb$

Spectroscopy was performed at six places on each crystal, roughly evenly distributed along the axis. Variations arose from the fact that some of the samples had broken, and positioning of the sample pieces had to be done to cover the ~0.5cm hole in the mounting plate for the spectroscopy. Distance was measured to

the center of the aperture, but spectroscopy measurements are impacted by a much larger area (0.5cm x 0.5cm) as compared to the point-like electron microprobe measurements.

Figure 3-2 and Figure 3-3 plot the FTIR and UV-VIS data for the $Ga_{70}In_{30}Sb$ crystal. The percent of light transmitted (%T) is plotted versus the wave length. The data from the spectroscopes were output in terms of wave number, which is related to wavelength by $\lambda(\mu m) = 1/(wave\ number)$.

The $Ga_{70}In_{30}Sb$ crystal had a high and fairly constant gallium concentration near the head, requiring the use of UV-VIS spectroscopy to find the cutoff wavelength. However, $Ga_{30}In_{70}Sb$ cutoff wavelengths were largely in the range of the FTIR. In Figure 3-4 it is notable that the farther away from the head of the crystal the measurements were taken, the greater the cutoff wavelength. The signal was corrected for the blank background. The cumulative experimental error is reported in the cutoff wavelength plot shown in Figure 3-6.

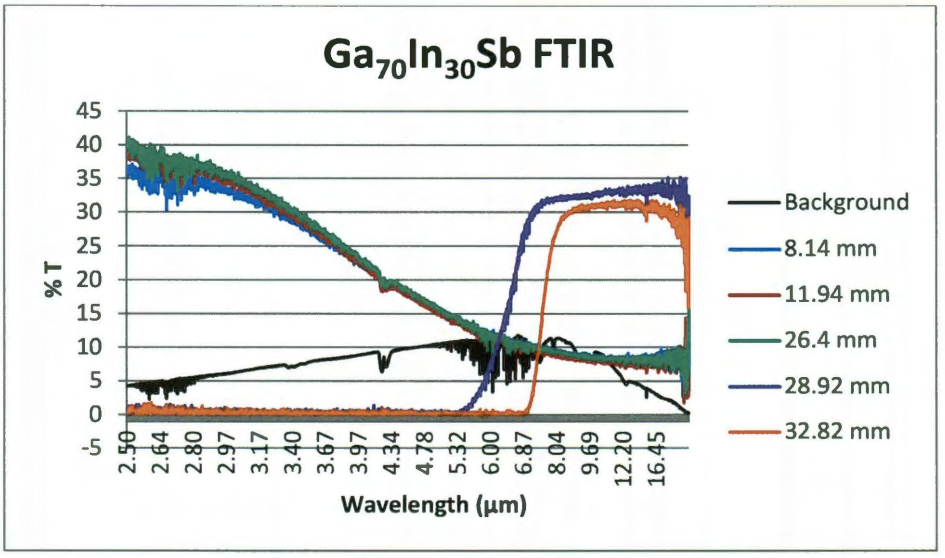

Figure 3-2 Plot of FTIR data for $Ga_{70}In_{30}Sb$

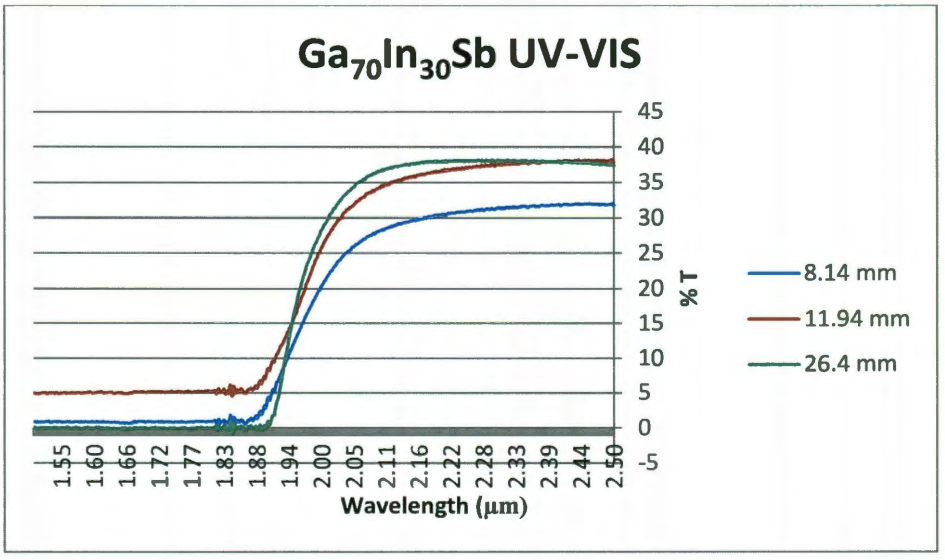

Figure 3-3 The UV-VIS data for $Ga_{70}In_{30}Sb$

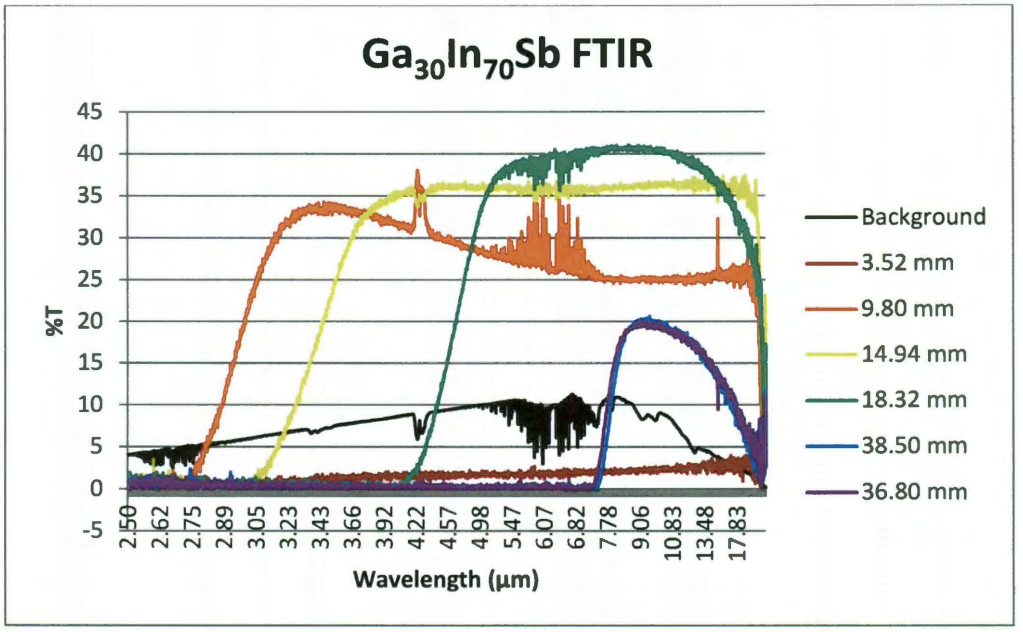

Figure 3-4 The FTIR plot for $Ga_{30}In_{70}Sb$

3.4. Cutoff Wavelength vs. Composition and Bandgap Energy

Table 3-2 provides the cutoff wavelength for the $Ga_{70}In_{30}Sb$ and the corresponding atomic percentage of gallium measured by EMP at that distance from the head of the crystal. Tables for $Ga_{50}In_{50}Sb$, and $Ga_{30}In_{70}Sb$ can be found in Appendix 5.3. From the tables a trend is relatively clear. As the atomic percentage of gallium decreases, the cutoff wavelength increases. This correlation also ties directly to the bandgap energy of the crystal – as the percentage of gallium decreases, which increases the cutoff wavelength of the sample, the bandgap energy is observed to decrease. These trends are also seen in Table 5-1 and Table 5-2 though there are two notable exceptions, one discussed here and one discussed in the appendix.

Distance from head (mm)	Wavelength of peak of derivative (μm)	% Ga (atomic)	Bandgap energy (eV)
8.14	1.95	47.35	0.635897
11.94	1.954	47.37	0.634596
26.4	1.936	44.97	0.640496
32.98	2.5873	36.47	0.479264
38.5	5.2493	11.63	0.236222
42.8	6.993	1.63	0.17732

Table 3-2 Spectroscopy data for $Ga_{70}In_{30}Sb$, showing the distance from the head, cut-off wavelength, atomic percentage of gallium, and the calculated bandgap energy

The exception in the $Ga_{70}In_{30}Sb$ sample is observed at 26.40 mm from the head. The cutoff wavelength decreased from the value measured at 11.94mm, despite having a lower atomic concentration of gallium at the 26.40mm measurement. However, this variation is small and is within the error of the measurement seen in the InSb sample. Furthermore, this portion of the $Ga_{70}In_{30}Sb$ crystal had broken into many pieces, making accurate measurements of distance difficult. The crystal was reconstructed on a sample mount for measurement of these distances.

With these variations explained, a plot of bandgap energy versus gallium concentration for all three crystals can be seen in Figure 3-5. This figure confirms the correlation between gallium concentration in the crystal and the cutoff wavelength found through spectroscopy. The error bars were constructed from the electron microprobe data. Taking the microprobe measurement from the closest mm to the spectroscopy measurement (i.e. for a spectroscopy measurement at 42.8 mm the microprobe data from 43 mm) was the centerpoint. The two ends of the error bars were the maximum and minimum values of the microprobe measurement for 2 millimeters around the centerpoint. Thus with a centerpoint at 43mm, the range of microprobe data used was 41-45 mm.

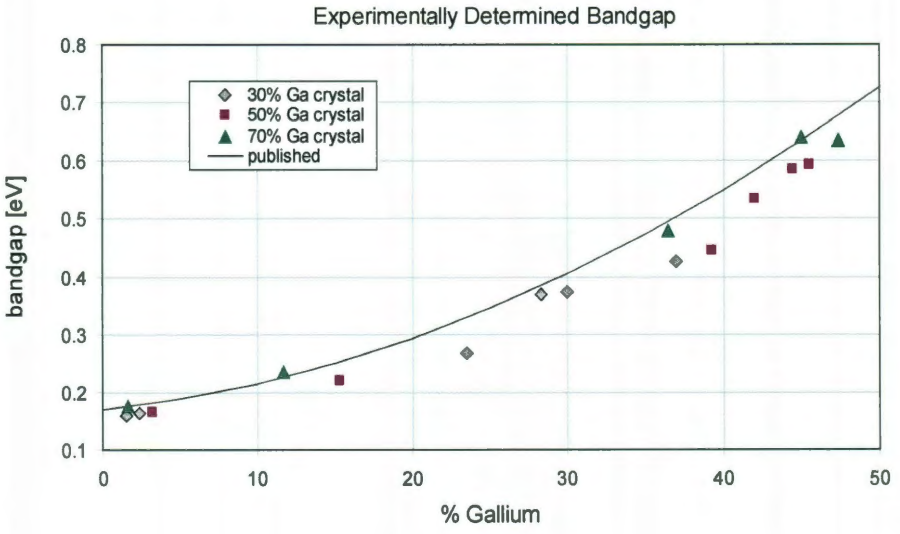

Figure 3-5 Plot of bandgap energy versus gallium percentage, using crystals of 30% Ga, 50% Ga, and 70% Ga measured at different horizontal locations compared to bowing parameter from [23]

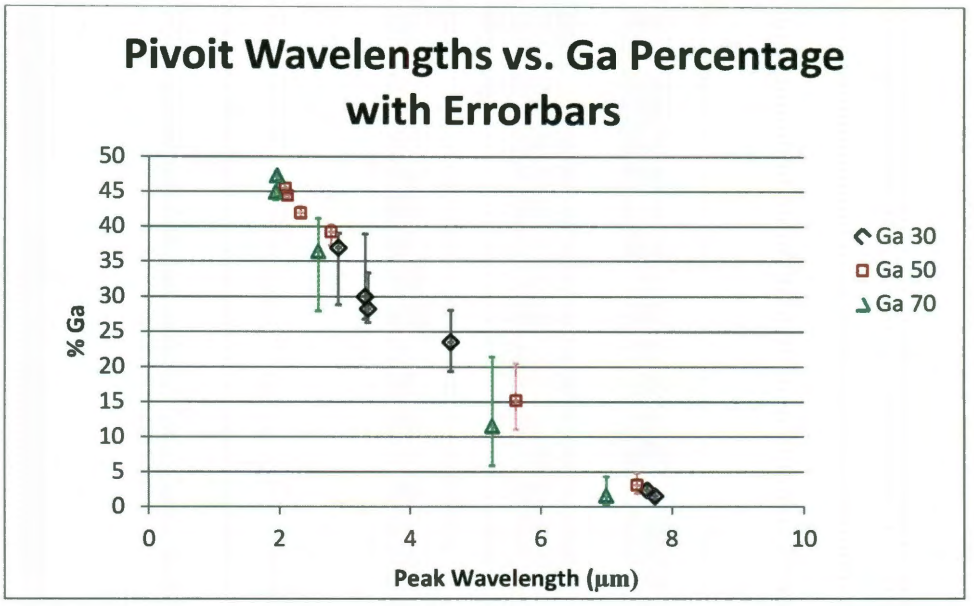

Figure 3-6 Cumulative Error bars for Gallium percentage

3.5. **Advanced Growth Techniques**

As detailed in [6], a large crystal was also grown using horizontal Travelling Heater Method by collaborators at Hanscom Air Force Base. It was not a true pseudobinary growth experiment, as excess indium was introduced to act as a solvent and encourage a more uniform composition in the grown crystal. The growth velocity was limited to 1.2 mm/day and the crystal was allowed to grow for roughly 80 days until it reached a length of 100 mm. The slow growth rate in this experiment allowed sufficient time for diffusion of solute through the In solvent, producing a very uniform final composition, as can be seen in Figure 3-7.

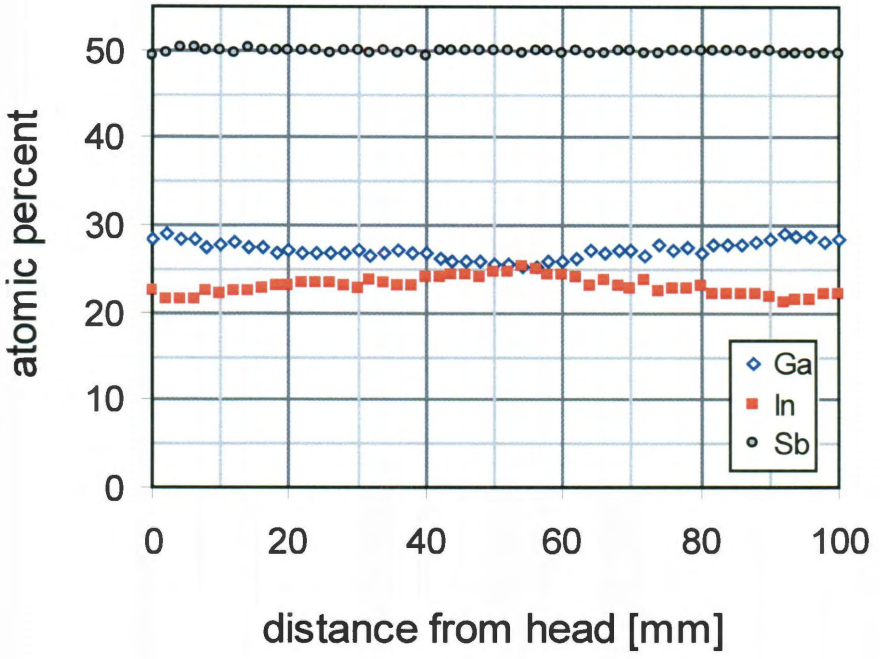

Figure 3-7 EMP data from the HTHM crystal, also found in [6]

Although the composition is remarkably uniform over the length, the growth of this moderately sized crystal took nearly three months to complete. Therefore a model to predict the composition, which can be run in hours to demine initial compositions for the charge and growth method, would be very useful.

Chapter 4

Modeling the Solidification for Well-mixed Bridgman Growth

Growth of an alloy is governed by mass conservation and transport, and these also dictate the composition distribution in the final product. The Scheil equation, Equation 4-1 governs the solidification of a melt when the melt remains well-mixed throughout the process. In the Scheil equation x_l is the concentration of solute in the liquid, x_s is the concentration of solute in the solid, and f_s is the position of the interface as a fraction of total length. Using this equation and the method described by Jacobs [24], an ideal solution, pseudobinary phase diagram can be constructed to determine the distribution of solute in the crystal.

$$(x_l - x_s)df_s = (1 - f_s)dx_l$$

Equation 4-1

For the $Ga_{1-x}In_xSb$ pseudobinary system the corresponding pseudobinary phase diagram was constructed using the values found in Sommelet and Lichter [25] with melting point temperatures of $T_{M,InSb}$ =524 °C and $T_{M,GaSb}$=712 °C, and with enthalpies of fusion $\Delta H_{f,InSb}$=11.41 kcal/mol (47,739 kJ/kmol) and $\Delta H_{f,GaSb}$=15.56 kcal/mol (65,103 kJ/kmol). These values were also used by Foster and Woods [26].

The well-mixed assumption for the melt is valid for the crystals grown and described in Chapter 2. This is because well-mixed melts can be obtained with sufficiently slow growth rates to allow for complete diffusion in a stagnant melt, with strong convective mass transport, or direct stirring of the melt with baffles, fins, or magnetic fields. The Bridgman grown crystals described above were grown with very slow growth rates and moderate melt convection [27].

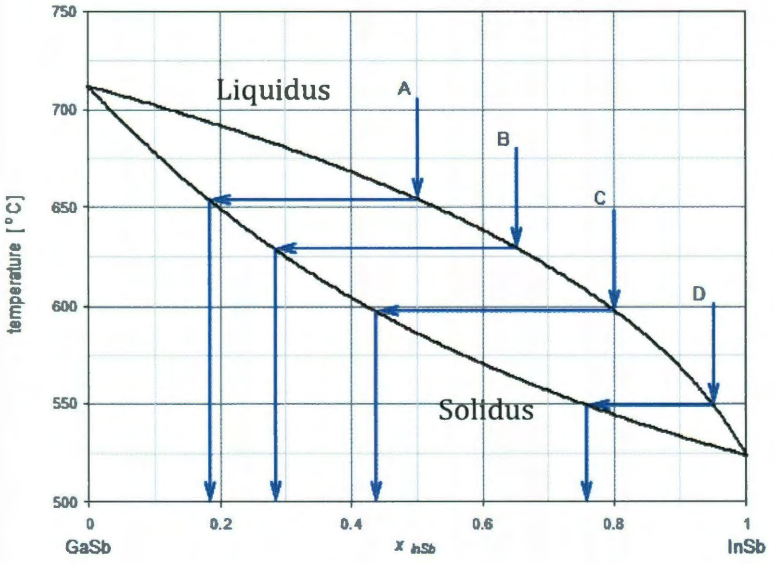

Figure 4-1 An ideal solution model pseudobinary phase diagram for $Ga_{1-x}In_xSb$

Figure 4-1 shows a pseudobinary phase diagram for $Ga_{1-x}In_xSb$ formed using the method described by Jacobs [24]. The blue lines detail the growth of a crystal from a non-replenishing melt solidified directionally from point A to D. In this example the melt begins with a composition of $Ga_{0.50}In_{0.50}Sb$ (point A), leading to the first solidification occurring at a mole fraction of $x_{InSb} \approx 0.18$ and corresponding to an atomic composition of roughly 41% Ga. The melt is then slightly gallium-depleted, corresponding to a higher mole fraction of InSb. Eventually, this decrease in gallium will drive the melt to the composition at point B, corresponding to a mole fraction of $x_{InSb} \approx 0.65$ in the melt. This causes the crystal to solidify with a mole fraction of $x_{InSb} \approx 0.29$ and 35.5% Ga. Again, this further depletes the gallium in the melt moving the composition to point C. Note that for points A through C, the resulting grown crystal is gallium-rich. Heavy gallium depletion in the melt, such as that at point D, is required before an indium-rich section of crystal can be grown. This also indicates that in a non-replenishing melt, the grown crystal will undergo a sudden composition change at some point, and this phenomenon is seen in the electron microprobe data (see Figure 3-1, and Figure 5-1, and Figure 5-2 in Appendix 5.1).

Unfortunately, the ideal solution model does not predict this sudden composition change very accurately, suggesting that the actual shape of the true pseudobinary diagram is distinctly different from the ideal model. This is discussed in sections 4.1 and 4.2

4.1. **Ideal Solution Model**

An ideal solution model assumes that the interaction energies between different particles (atoms or molecules) in the solution are equal. As described in Scheel and Capper [28], this means that for two particles A and B the interaction energies in an ideal solution are given by Equation 4-2.

$$\varepsilon_{AA} = \varepsilon_{BB} = \varepsilon_{AB}$$

Equation 4-2

The free energy of mixing per unit mole of an ideal binary was described by Equation 1 in Foster and Woods [26], and is included here as Equation 4-3. For an ideal solution the heat of mixing is zero, leading to the chemical change in potential also described by Foster and Woods [26] and reproduced below as Equation 4-4 (a) and (b). In the following equations, the different particles or materials are indicated by subscripts 1 and 2. Superscript l and s refer to liquid and solid phases, respectively.

$$\Delta F^{M(l)} = RT(x_1 \ln x_1 + x_2 \ln x_2)$$

Equation 4-3

$$\Delta\mu_1^{\,l} = RT\ln x_1 \qquad (a)$$
$$\Delta\mu_2^{\,l} = RT\ln x_2 \qquad (b)$$

Equation 4-4

The solidus and liquidus lines for the ideal pseudobinary diagram can then be calculated from Equation 4-5 and Equation 4-6 respectively.

$$x^s{}_{id} = \frac{\left\{1 - \exp\left[-\frac{L_1(T-T_1)}{RTT_1}\right]\right\}}{\left\{\exp\left[\frac{L_2(T-T_2)}{RTT_2}\right] - \exp\left[\frac{L_1(T-T_1)}{RTT_1}\right]\right\}}$$

Equation 4-5

$$x^l{}_{id} = \frac{\left\{1-\exp\left[-\frac{L_1(T-T_1)}{RTT_1}\right]\right\}}{\left\{\exp\left[-\frac{L_2(T-T_2)}{RTT_2}\right]-\exp\left[-\frac{L_1(T-T_1)}{RTT_1}\right]\right\}}$$

Equation 4-6

4.2. Improved pseudobinary phase diagram and the regular solution model

Unsurprisingly, most materials do not exactly follow the ideal solution model. Most noticeably, the heat of mixing is not zero, primarily due to changes in van der

Waals forces and the formation of chemical bonds between neighbors in the liquid phase. Including such non-idealities gives rise to the regular solution model.

Foster and Woods [26], expressed these non-idealities as Bx_1x_2 where x_1 and x_2 are the mole fractions of the components and B is an interaction parameter. This interaction parameter contains multiple contributions to non-ideality. In a liquid it covers both enthalpy and entropy contributions, and for a solid it also covers distortion energy. Representing this interaction parameter as B^l for liquids and B^s for solids, Equation 4-3 becomes Equation 4-7 (free energy of mixing equation) with the addition of these non-idealities. Likewise, adding these non-idealities to Equation 4-4 gives Equation 4-8 (chemical change in potential equations).

$$\Delta F^{M(l)} = RT(x_1 \ln x_1 + x_2 \ln x_2) + B^l x_1 x_2$$

Equation 4-7

$$\Delta\mu_1^{\,l} = RT \ln x_1 + B^l x_2^{\,2} \qquad (a)$$
$$\Delta\mu_2^{\,l} = RT \ln x_2 + B^l x_1^{\,2} \qquad (b)$$

Equation 4-8

Using the relationship $\mu = RT \ln a = RT \ln x + RT \ln \gamma$, where a is the activity, the activity coefficient γ can be found. These are defined by Equation 4-9 below for activity in the liquid.

$$\ln \gamma_1^{\,l} = \left(\frac{B^l}{RT}\right) x_2^{\,2} \qquad (a)$$

$$\ln \gamma_2^{\,l} = \left(\frac{B^l}{RT}\right) x_1^{\,2} \qquad (b)$$

Equation 4-9

Due to the fact that B^s incorporates additional effects it should be larger than B^l [26]. This leads to Equation 4-10 for the free energy of the solid per unit mole and Equation 4-11 for the activity coefficients in the solid.

$$\Delta F^{M(s)} = RT(x_1 \ln x_1 + x_2 \ln x_2) + x_1 L_1 \left(\frac{T}{T_1} - 1\right) + x_2 L_2 \left(\frac{T}{T_2} - 1\right) + B^s x_1 x_2$$

Equation 4-10

$$\ln \gamma_1^{\,s} = \left(\frac{B^s}{RT}\right) x_2^{\,2} \qquad (a)$$

$$\ln \gamma_2^{\,s} = \left(\frac{B^s}{RT}\right) x_1^{\,2} \qquad (b)$$

Equation 4-11

Foster and Woods also gave the conditions for equilibrium in [26], reproduced below as Equation 4-12 and Equation 4-13.

$$RT\ln(1-x^l)+B^l(x^l)^2 = RT\ln(1-x^s)+B^s(x^s)^2+\frac{L_1(T-T_1)}{T_1}$$

Equation 4-12

$$RT\ln\left(\frac{x^l}{1-x^l}\right)+B^l(1-2x^l) = RT\ln\left(\frac{x^s}{1-x^s}\right)+B^s(1-2x^s)-\frac{L_1(T-T_1)}{T_1}+\frac{L_1(T-T_2)}{T_2}$$

Equation 4-13

From these equations the corrected pseudobinary phase diagram of the regular solution is calculated using $B^s = 0$and $B^l \approx RT = 1$ from [26].

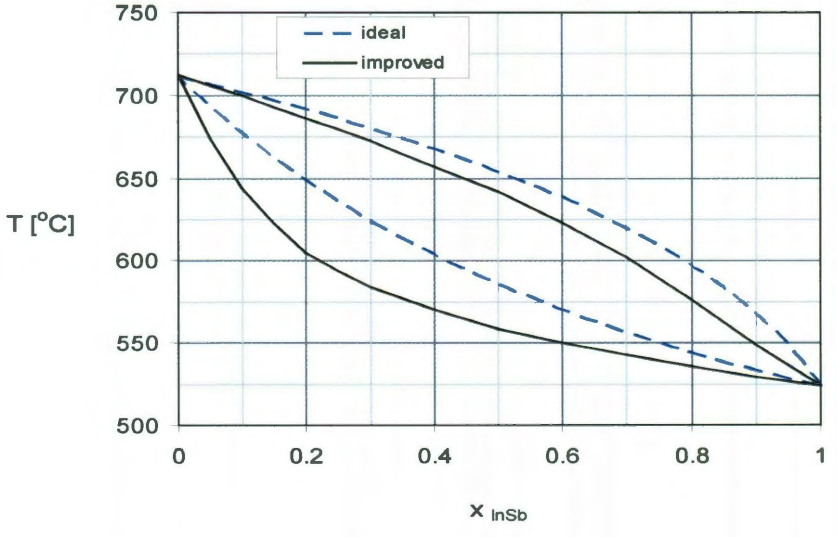

Figure 4-2 The ideal and regular solution pseudobinary phase diagrams for $Ga_{1-x}In_xSb$

Plotting the two models and comparing the ideal and regular solution phase diagrams, as seen in Figure 4-2, there are some notable differences. In the regular solution model, the solidus curve has a very distinctive bend at x_{InSb}=0.2 (i.e. x_{GaSb}=0.8). Additionally the solidus and liquidus lines in the regular solution model are lower in temperature than the ideal model at all but the end points.

The equations for the solidus and liquidus mole fractions (as a function of temperature) of the ideal model for InSb-GaSb are Equation 4-14 and Equation 4-15.

$$x_{InSb,s} = x_{InSb,l} \exp\left(\frac{\Delta H_{InSb}(1-T)/T_{M,InSb}}{RT}\right)$$

Equation 4-14

$$x_{InSb,l} = \frac{1-\exp\left(\frac{\Delta H_{GaSb}(1-T)/T_{M,GaSb}}{RT}\right)}{\exp\left(\frac{\Delta H_{InSb}(1-T)/T_{M,InSb}}{RT}\right)-\exp\left(\frac{\Delta H_{GaSb}(1-T)/T_{M,GaSb}}{RT}\right)}$$

Equation 4-15

For the regular solution model of InSb-GaSb, the liquidus mole fraction of InSb can be found from Equation 4-16. Given the liquidus mole fraction of InSb substituting into Equation 4-17 at the same temperature will give the solidus mole fraction of InSb for the regular solution model.

$$\left(RT\ln(1-x_{s,InSb}) + RT(x_{s,InSb})^2 + \frac{\Delta H_{f,GaSb}(T-T_{M,GaSb})}{T_{M,GaSb}} \right) \frac{1}{RT} = \ln(1-x_{l,InSb})$$

Equation 4-16

$$RT\ln\left(\frac{x_{l,InSb}}{1-x_{l,InSb}}\right) - RT\ln\left(\frac{x_{s,InSb}}{1-x_{s,InSb}}\right) + RT(2x_{s,InSb}) + \frac{\Delta H_{f,GaSb}(T-T_{M,GaSb})}{T_{M,GaSb}} - \frac{\Delta H_{f,InSb}(T-T_{M,InSb})}{T_{M,InSb}} = RT$$

Equation 4-17

4.3. **Computational Modeling**

To compare the ability of the ideal and the regular solution models, Matlab programs were developed using the above equations to build both pseudobinary phase diagrams, by building a lookup table. To find the expected composition of the grown crystal along its length, a recursive loop was written to perform the stepping described by Figure 4-1. In this case, Bridgman growth was modeled. The materials were fully melted and well-mixed, and solidification occurred from one end.

From the phase diagram tables and liquidus composition, the temperature was interpolated. Using the temperature, the solidus mole fraction of InSb was calculated. The total number of moles of GaSb plus the total number of moles of InSb in the system were divided by the total number of N 'sliver' solidification steps. A larger N meant that more iterations were performed with fewer moles of material

being solidified out each time, increasing the resolution of the model. From the mole fraction of InSb for the solid, and the solidification step size, the number of moles of InSb solidified in that block was found. The moles of GaSb which had been rejected from the solute and solidified were then calculated at that time step. Subtracting these values from the previous amounts of InSb and GaSb in the liquid lead to the updated number of moles and the mole fractions of both GaSb and InSb in the melt. This process was repeated until the entirety of the melt was crystallized. Once the crystal was fully solidified, the electron microprobe data was added to the plot to see how well the models compared to the experimental data.

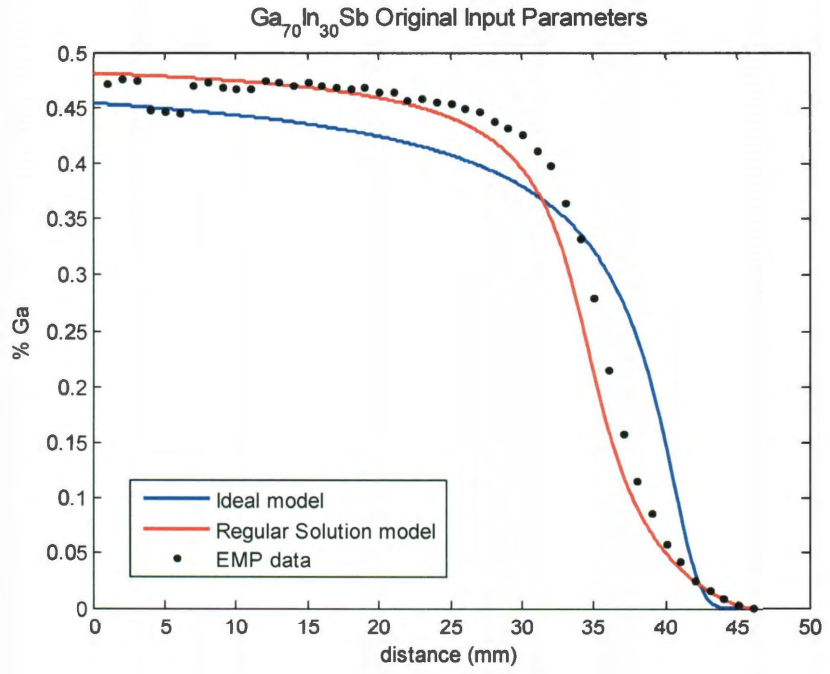

Figure 4-3 Comparison of Ideal and Regular Solution models to EMP data for $Ga_{70}In_{30}Sb$

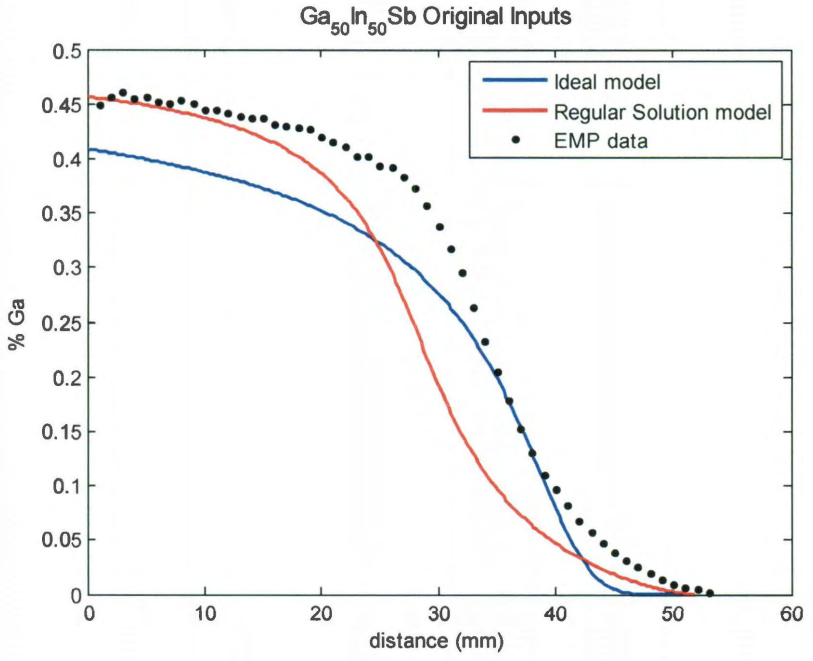

Figure 4-4 Comparison of Ideal and Regular Solution models to EMP data for $Ga_{50}In_{50}Sb$

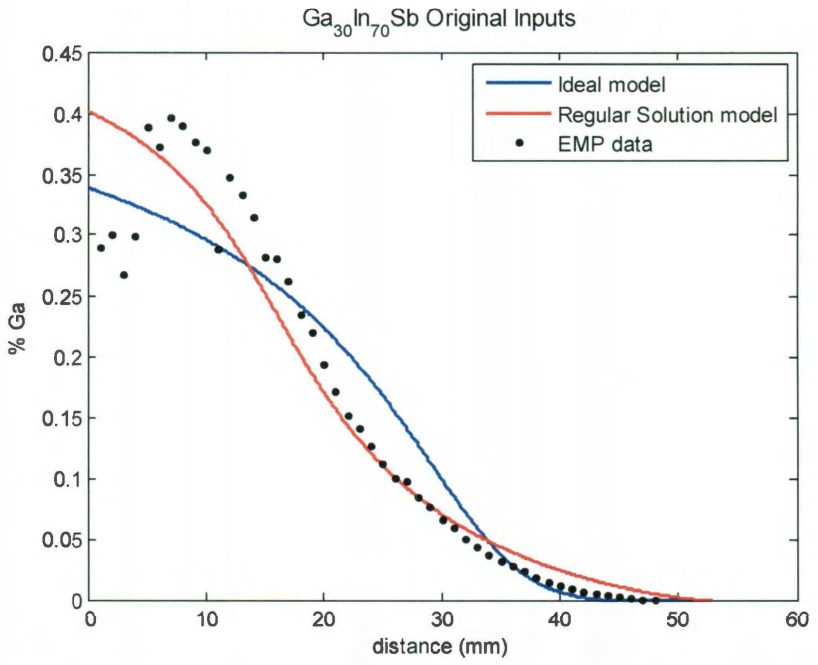

Figure 4-5 Comparison of Ideal and Regular Solution models to EMP data for $Ga_{30}In_{70}Sb$

Figure 4-3 shows that the regular solution model is much more accurate for predicting the crystal growth. In all three situations (see also Figure 4-4 and Figure 4-5), the shape of the regular solution model is much closer to the EMP data then that of the ideal solution model. While the regular solution does not exactly overlay the EMP data, this is likely due to the fact that the initial composition of the melt was not exactly 70% GaSb and 30% InSb (or 50-50 or 30-70). There is error associated with measuring out the moles of each element. As mentioned in 2.2 Horizontal Growth, the sample was ground and etched after synthesis. It is unlikely that the elements were lost in exact proportion to the desired melt composition, so the actual melt may have been closer to $Ga_{68}In_{32}Sb$ instead of the desired composition of $Ga_{70}In_{30}Sb$. This variation can be seen in the EMP numerical data. The mean value of

gallium in the $Ga_{70}In_{30}Sb$ sample was 0.3501, leading to an actual melt composition of $Ga_{70.02}In_{29.98}Sb$.

Desired Crystal	Modified GaSb(kmol)	Modified InSb (kmol)	Resultant Crystal
$Ga_{70}In_{30}Sb$	73.02	31.28	$Ga_{70.02}In_{29.98}Sb$
$Ga_{50}In_{50}Sb$	57.35	42.65	$Ga_{57.34}In_{42.66}Sb$
$Ga_{30}In_{30}Sb$	30.60	65.37	$Ga_{31.88}In_{68.12}Sb$

By modifying the initial composition of the melt for the computations, better agreement between the EMP data and regular solution model occurs for $Ga_{50}In_{50}Sb$ and $Ga_{30}In_{70}Sb$ (see Figure 4-7 and Figure 4-8). With the $Ga_{70}In_{30}Sb$ crystal, the initial values were exceedingly close to the desired amount, but even this small variation in the input amounts significantly altered the predicted crystal composition. This sensitivity is exacerbated in high gallium crystals.

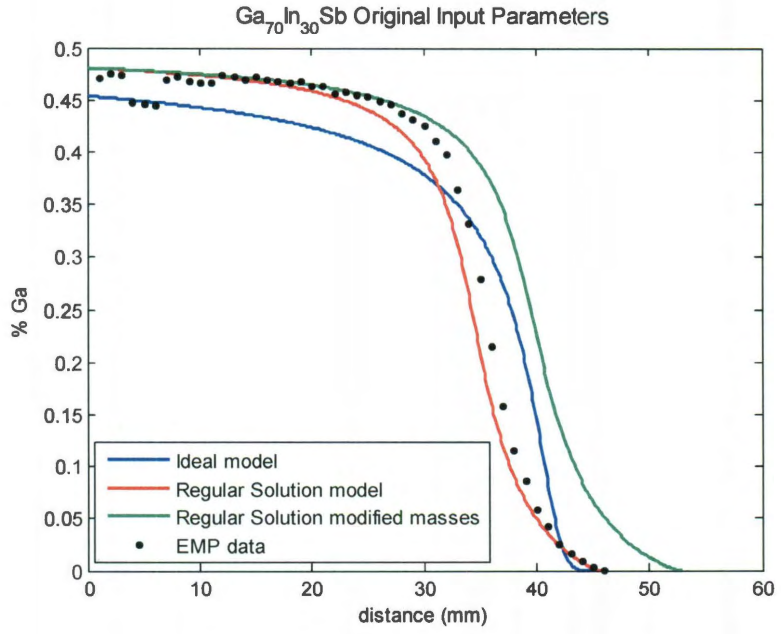

Figure 4-6 Comparison of regular solution model with modified beginning massses to the Ideal model, Regular Solution model, and EMP data for $Ga_{70}In_{30}Sb$

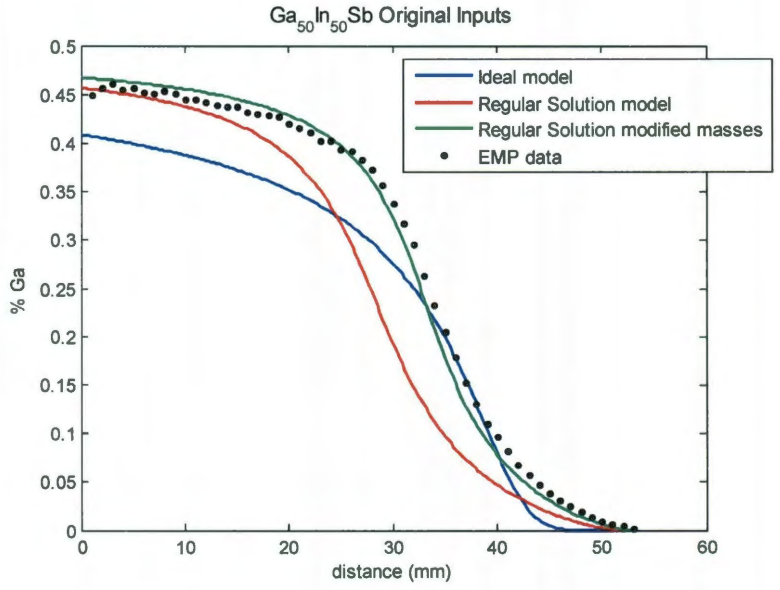

Figure 4-7 Comparison of Regular Solution model with modified beginning massses to the Ideal model, Regular Solution model, and EMP data for $Ga_{50}In_{50}Sb$

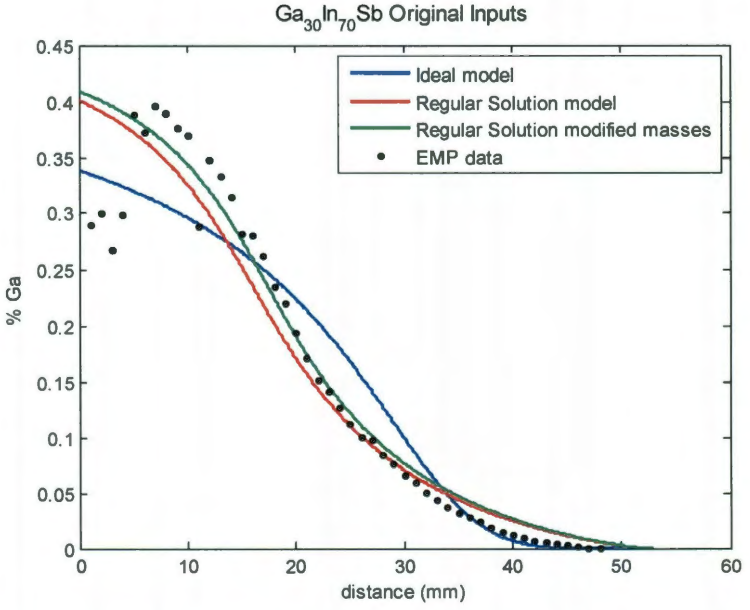

Figure 4-8 Comparison of Regular Solution model with modified beginning massses to the Ideal model, Regular Solution model, and EMP data for $Ga_{30}In_{70}Sb$

References

[1] V. F. S. Yip and W. R. Wilcox, "Growth of GaAs, GaxIn1-xSb and GaxAl1-xAs by the travelling heater method," *Materials Research Bulletin*, vol. 11, no. 8, pp. 895-901, Aug. 1976.

[2] P. S. Dutta, "III-V Ternary bulk substrate growth technology: a review," *Journal of Crystal Growth*, vol. 275, no. 1-2, pp. 106-112, Feb. 2005.

[3] Z. Yin and X. Tang, "A review of energy bandgap engineering in III-V semiconductor alloys for mid-infrared laser applications," *Solid-State Electronics*, vol. 51, no. 1, pp. 6-15, Jan. 2007.

[4] I. Melngailis, "Small bandgap semiconductor infrared detectors," *Journal of Luminescence*, vol. 7, pp. 501-523, 1973.

[5] C. E. Chang and W. R. Wilcox, "Localized interface breakdown in zone melting and the travelling heater method," *Journal of Crystal Growth*, vol. 21, no. 2, pp. 182-186, Feb. 1974.

[6] B. C. Houchens, P. Becla, S. E. Tritchler, A. J. Goza, and D. F. Bliss, "Crystal growth of bulk ternary semiconductors: Comparison of GaInSb growth by horizontal Bridgman and horizontal traveling heater method," *Journal of Crystal Growth*, vol. 312, no. 8, pp. 1090-1094, Apr. 2010.

[7] V. F. S. Yip, C. E. Chang, and W. R. Wilcox, "Heat and mass transfer in the travelling heater method of crystal growth," *Journal of Crystal Growth*, vol. 29, no. 1, pp. 69-74, May. 1975.

[8] H. Nakamura, Y. Hanaue, H. Kato, K. Kinoshita, and S. Yoda, "A one-dimensional model to predict the growth conditions of InxGa1-xAs alloy crystals grown by the traveling liquidus-zone method," *Journal of Crystal Growth*, vol. 258, no. 1-2, pp. 49-57, Oct. 2003.

[9] K. Kinoshita, H. Kato, M. Iwai, T. Tsuru, Y. Muramatsu, and S. Yoda, "Homogeneous In0.3Ga0.7As crystal growth by the traveling liquidus-zone method," *Journal of Crystal Growth*, vol. 225, no. 1, pp. 59-66, May. 2001.

[10] S. Adachi et al., "Homogeneous SiGe crystals grown by using the traveling liquidus-zone method," *Journal of Crystal Growth*, vol. 280, no. 3-4, pp. 372-377, Jul. 2005.

[11] S. Adachi et al., "Latent heat effect on growth rate in the traveling liquidus-zone method," *Journal of Crystal Growth*, vol. 271, no. 1-2, pp. 22-28, Oct. 2004.

[12] S. Adachi et al., "Numerical analysis of growth rates in the traveling liquidus-zone method," *Journal of Crystal Growth*, vol. 270, no. 1-2, pp. 42-49, Sep. 2004.

[13] A. Mitric et al., "Growth of Ga(1-x)InxSb alloys by Vertical Bridgman technique under alternating magnetic field," *Journal of Crystal Growth*, vol. 287, no. 2, pp. 224-229, Jan. 2006.

[14] C. Stelian, Y. Delannoy, Y. Fautrelle, and T. Duffar, "Bridgman growth of concentrated GaInSb alloys with improved compositional uniformity under alternating magnetic fields," *Journal of Crystal Growth*, vol. 275, no. 1-2, p. e1571-e1578, Feb. 2005.

[15] H. J. Kim, A. Chandola, R. Bhat, and P. S. Dutta, "Forced convection induced thermal fluctuations at the solid-liquid interface and its effect on the radial alloy distribution in vertical Bridgman grown Ga1-xInxSb bulk crystals," *Journal of Crystal Growth*, vol. 289, no. 2, pp. 450-457, Apr. 2006.

[16] A. Tanaka, T. Yoneyama, M. Kimura, and T. Sukegawa, "Control of GaInSb alloy composition grown from ternary solution," *Journal of Crystal Growth*, vol. 186, no. 3, pp. 305-308, Mar. 1998.

[17] P. S. Dutta and A. G. Ostrogorsky, "Suppression of cracks in InxGa1-xSb crystals through forced convection in the melt," *Journal of Crystal Growth*, vol. 194, no. 1, pp. 1-7, Nov. 1998.

[18] T. Maekawa, Y. Sugiki, S. Matsumoto, S. Adachi, S. Yoda, and K. Kinoshita, "Numerical analysis of crystal growth of an InAs-GaAs binary semiconductor by the Travelling Liquidus-Zone method under microgravity conditions," *International Journal of Heat and Mass Transfer*, vol. 47, no. 21, pp. 4535-4546, Oct. 2004.

[19] P. S. Dutta and A. G. Ostrogorsky, "Segregation of Ga in Ge and InSb in GaSb," *Journal of Crystal Growth*, vol. 217, no. 4, pp. 360-365, Aug. 2000.

[20] A. Mitric, T. Duffar, V. Corregidor, L. C. Alves, and N. P. Barradas, "Growth of GaInSb concentrated alloys under alternating magnetic field," *Journal of Crystal Growth*, vol. 310, no. 7-9, pp. 1424-1432, Apr. 2008.

[21] B. Ganapathysubramanian and N. Zabaras, "On the control of solidification using magnetic fields and magnetic field gradients," *International Journal of Heat and Mass Transfer*, vol. 48, no. 19-20, pp. 4174-4189, Sep. 2005.

[22] V. Corregidor et al., "Compositional and structural characterisation of GaSb and GaInSb," *Nuclear Instruments and Methods in Physics Research Section B: Beam Interactions with Materials and Atoms*, vol. 240, no. 1-2, pp. 360-364, Oct. 2005.

[23] I. Vurgaftman, J. R. Meyer, and L. R. Ram-Mohan, "Band parameters for III–V compound semiconductors and their alloys," *Journal of Applied Physics*, vol. 89, no. 11, p. 5815, 2001.

[24] K. Jacobs, "Fundamentals of Equilibrium Thermodynamics of Crystal Growth," *Crystal Growth Technology: From Fundamentals and Simulation to Large-scale Production, Scheel, H. J. and Capper, P., eds., Wiley-VCH Verlag GmbH & Co. KGaA, Weinheim, Germany*, p. 505, 2008.

[25] P. Sommelet and B. D. Lic, "Thermal Properties of AIIIBV Compounds: Part I," *Transactions of AIME*, vol. 245, 1969.

[26] L. M. Foster and J. F. Woods, "Thermodynamic analysis of the III-V alloy semiconductor phasediagrams: I. InSb-Ga-Sb, InAs-GaAs, InP-GaP," *Journal of the Electrochemical Society*, vol. 118, no. 7, pp. 1175-1183, 1971.

[27] A. J. Goza, S. E. Tritchler, D. F. Bliss, and B. C. Houchens, "Thermodynamic modeling of bulk ternary alloy crystal growth: Comparison of experiments and theory for GaInSb alloys," *Journal of Crystal Growth*, vol. 337, no. 1, 60-64, 2011.
[28] H. J. Scheel and P. Capper, "Crystal Growth Technology," *Eds*, 2008.

Chapter 5

Appendix A: Additional data from the Bridgman growth and analysis

This section contains additional data from the analysis of the crystals grown at Hanscom Air Force Base. Due to the number of all the tables, FTIR, UV-VIS, and electron microprobe graphs for all three crystals, an exemplar was included in the body of the thesis while the data for the other crystals has been collected here.

5.1. Additional electron microprobe data

For $Ga_{30}In_{70}Sb$, the beginning of the crystal was highly polycrystalline, which can be seen in the randomness of the first 15 mm of the crystal in the microprobe data.

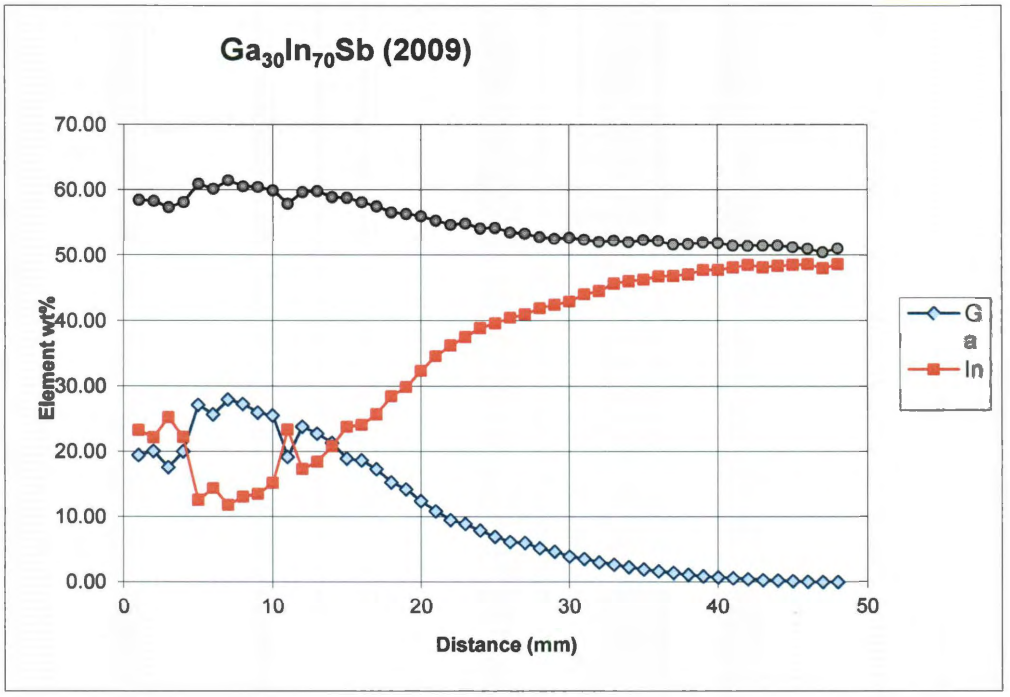

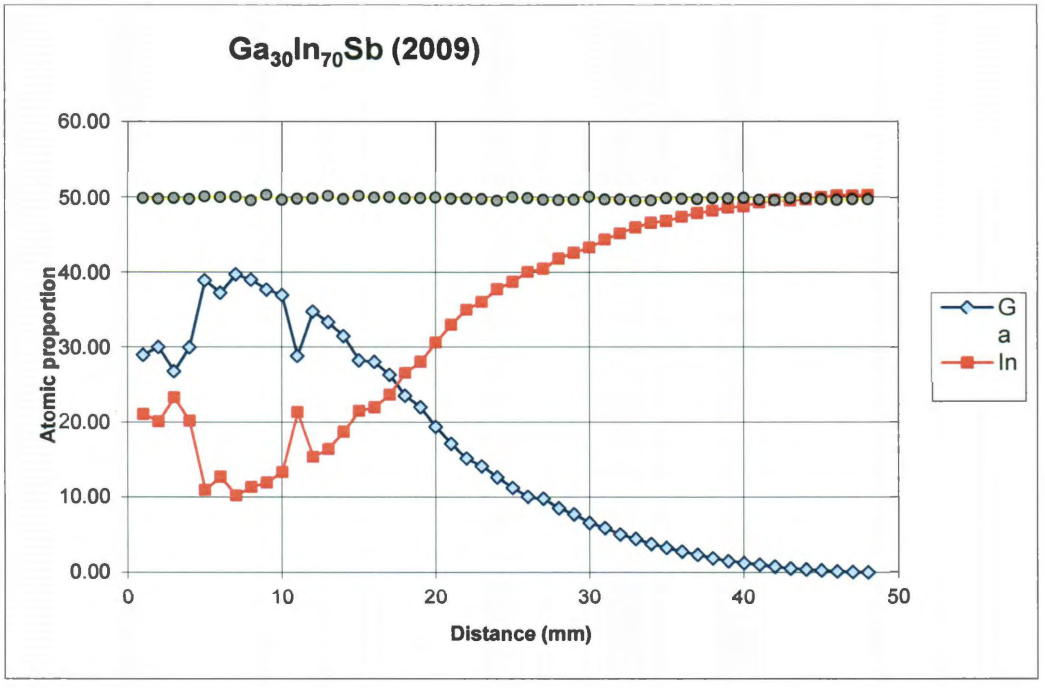

Figure 5-1 Electron microprobe data for $Ga_{30}In_{70}Sb$

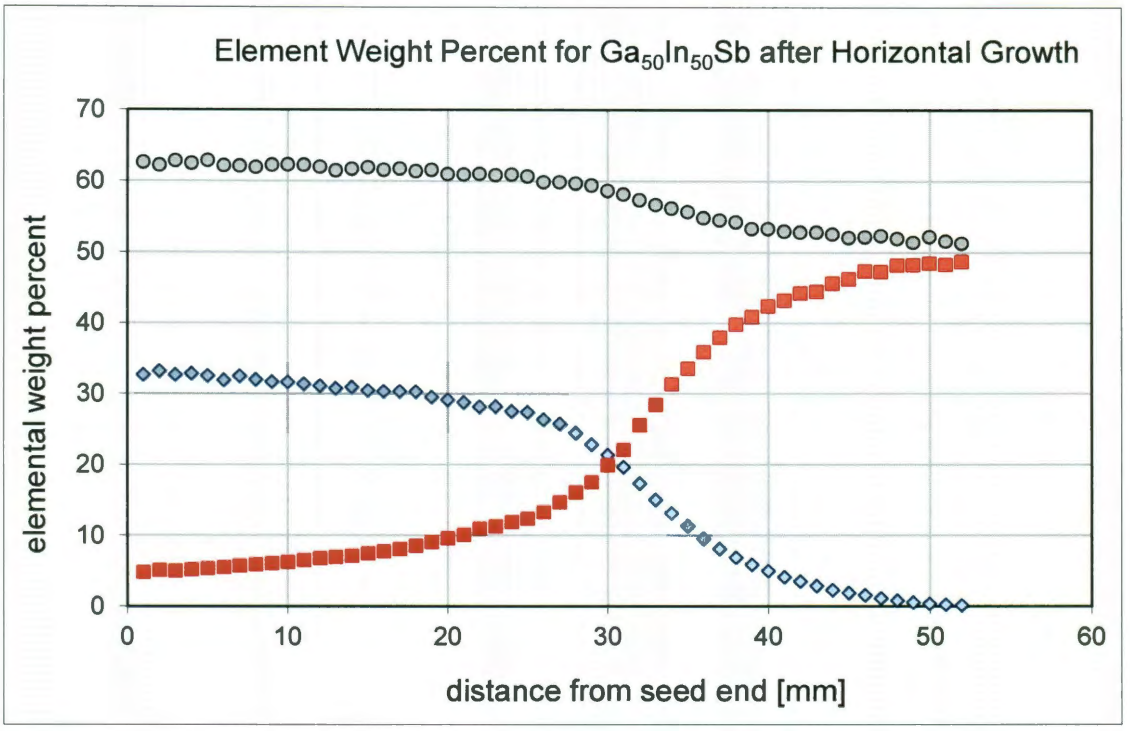

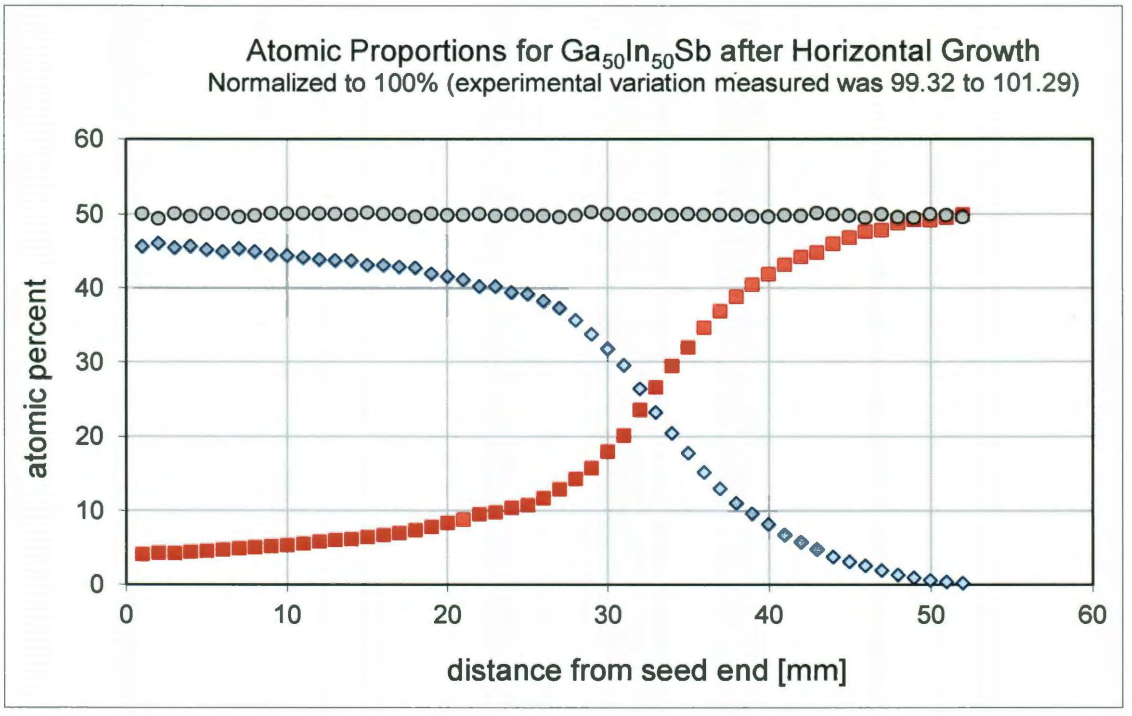

Figure 5-2 Electron microprobe data for $Ga_{50}In_{50}Sb$

5.2. **Additional FTIR and UV-VIS data**

For the $Ga_{30}In_{70}Sb$ case, the cutoff wavelengths were able to be measured using just the FTIR. This example easily shows how the peak wavelength increases along the length of the crystal, and when compared with Figure 5-1, it also increases with decreasing gallium content.

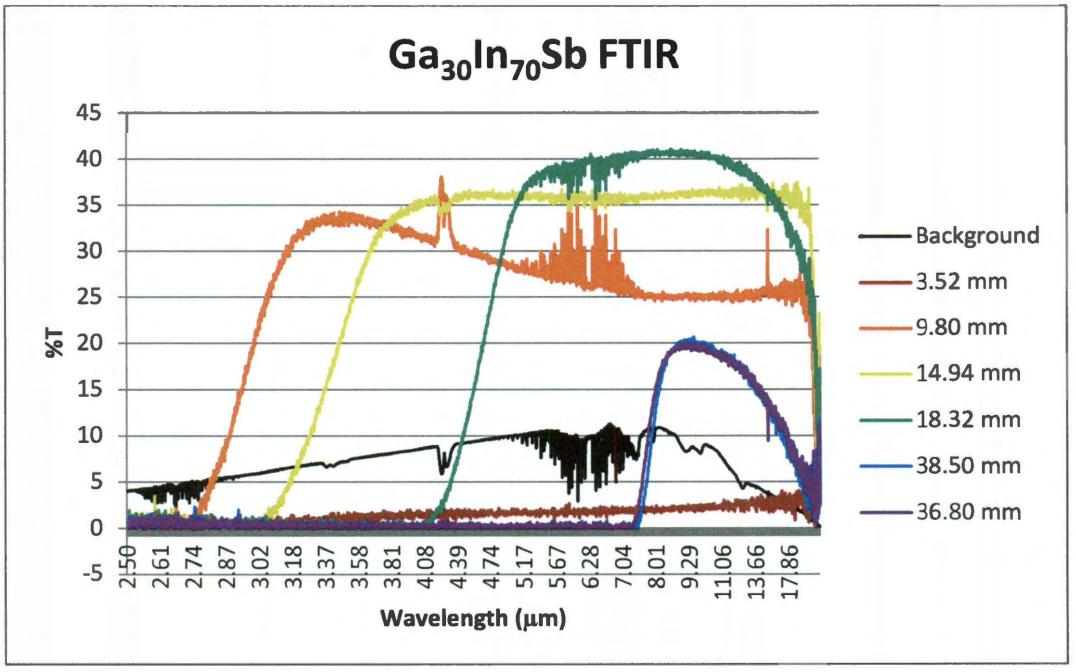

Figure 5-3 FTIR data for $Ga_{30}In_{70}Sb$

For $Ga_{50}In_{50}Sb$ both FTIR and UV-VIS was needed.

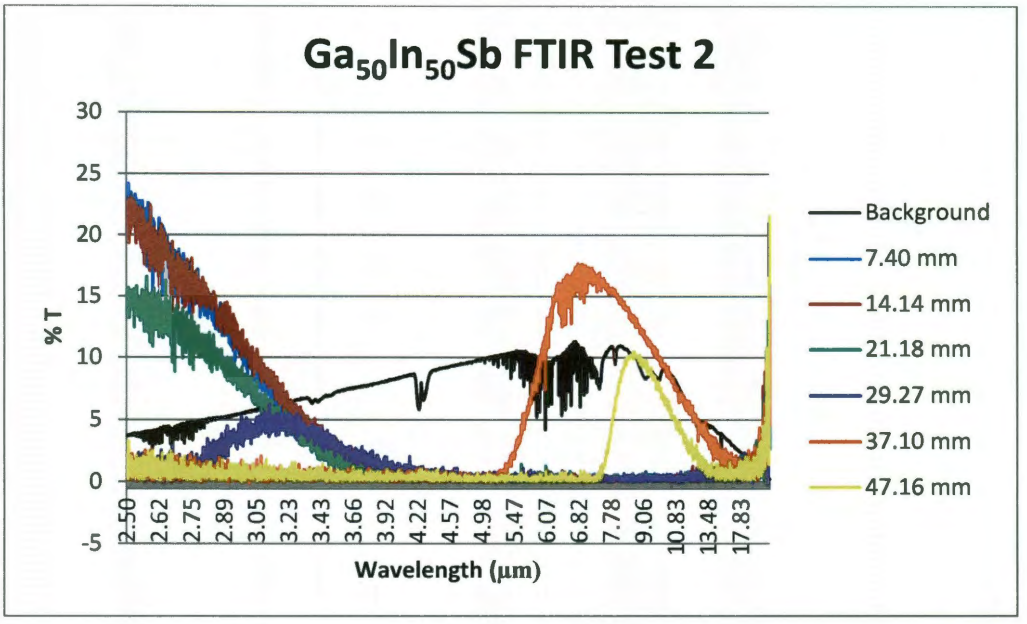

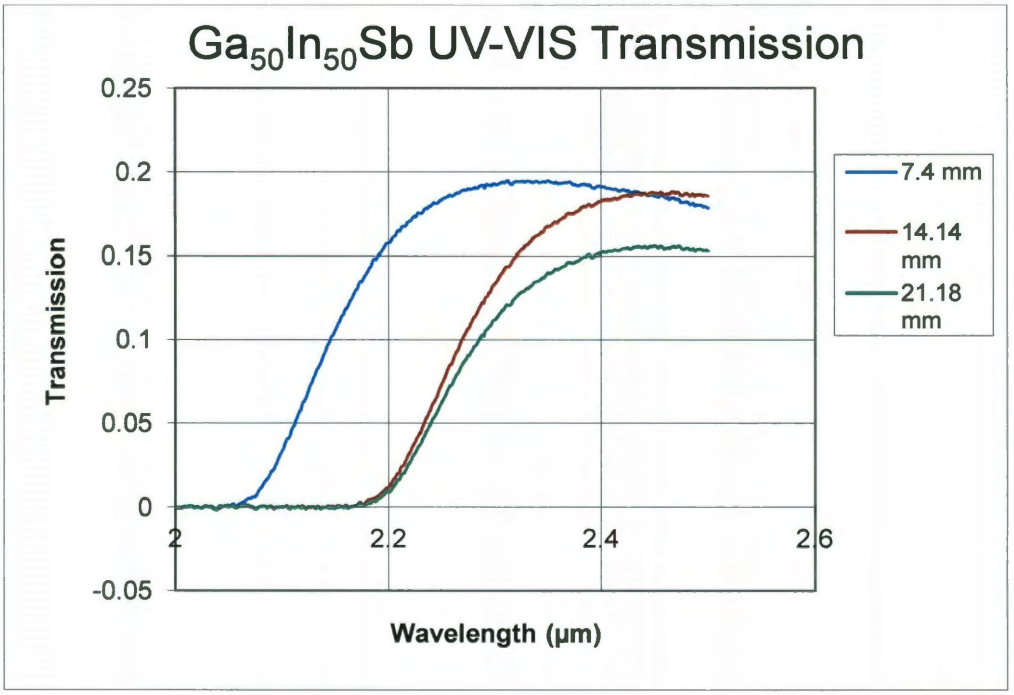

Figure 5-4 FTIR and UV-VIS data for $Ga_{50}In_{50}Sb$

5.3. Tables of cut-off wavelengths

Distance from head (mm)	Wavelength of peak of derivative (μm)	% Ga (atomic)	Bandgap energy (eV)
3.52	3.3113	30.00	0.3745
9.80	2.9011	36.98	0.4274
14.94	3.3568	28.28	0.3694
18.32	4.6232	23.54	0.2682
36.80	7.622	2.37	0.1627
38.50	7.7399	1.53	0.1602

Table 5-1 Spectroscopy data for $Ga_{30}In_{70}Sb$, showing the distance from the head, cut-off wavelength, atomic percentage of gallium, and the calculated bandgap energy

At one point in the $Ga_{30}In_{70}Sb$ crystal the bandgap energy increases slightly before continuing the general trend. This occurred at 3.52 mm from the head. The cutoff wavelength was higher than that at the next position measured, at 9.8 mm from the head, though the EMP data indicated gallium concentration was lower. However the EMP data also revealed that the sample was highly polycrystalline in

the area. This poor crystalline structure, coupled with the large aperture of the FTIR/UV-VIS produced inaccurate readings in this region.

Distance from head (mm)	Wavelength of peak of derivative (μm)	% Ga (atomic)	Bandgap energy (eV)
4.00	2.083	45.547	0.595295
11.98	2.115	44.476	0.586288
20.42	2.319	41.983	0.534713
26.82	2.7855	39.267	0.445162
37.50	5.618	15.273	0.220719
46.00	7.4627	3.162	0.16616

Table 5-2 Spectroscopy data for $Ga_{50}In_{50}Sb$, showing the distance from the head, cut-off wavelength, atomic percentage of gallium, and the calculated bandgap energy